Jolts in the Jade factory: A route for subduction fluids and their implications for mantle wedge seismicity

Samuel Angiboust, Jesus Muñoz-Montecinos, Aitor Cambeses, Tom Raimondo, Damien Deldicque, Antonio Garcia-Casco

Jolts in the Jade Factory: a Route for Subduction Fluids and their Implications for Mantle Wedge Seismicity

Samuel Angiboust [1]

Jesus Muñoz-Montecinos[1,2]

Aitor Cambeses [1,2]

Tom Raimondo [3]

Damien Deldicque [4]

Antonio Garcia-Casco[2,5]

[1] *Université de Paris, Institut de Physique du Globe de Paris, F-75005 Paris, France*
(corresponding author: angiboust@ipgp.fr)*

[2] *Department of Mineralogy and Petrology, Faculty of Sciences, University of Granada, Campus Fuentenueva s/n, 18002 Granada, Spain*

[3] *UniSA STEM, University of South Australia, GPO Box 2471, Adelaide SA 5001, Australia*

[4] *Laboratoire de Géologie, Ecole Normale Supérieure PSL, F-75005 Paris, France*

[5] *Instituto Andaluz de Ciencias de la Tierra, CSIC-Universidad de Granada, 18100 Armilla, Granada, Spain.*

Keywords

Subduction, Fluids, Jadeitite, Earthquakes, Mantle wedge, Foliated cataclasites

Abstract

An increasing number of seismological studies report transient seismicity clusters in the mantle wedge several kilometers above the subduction interface. Their physical significance with respect to subduction zone seismo-tectonics remains poorly understood. Jadeitites are known to form and/or be associated with mantle wedge serpentinites in the c. 30-70 km depth range, and thus may yield information on deformation mechanisms in this region of deep subduction environments. We herein document and compare brittle-viscous features recorded in jadeitites from Polar Urals (Russia), Kashin state (Myanmar) and Motagua fault region (Guatemala) – some of the most important jadeitite occurrences worldwide. In the Polar Urals we identified ultramafic-hosted pristine jadeitite-bearing veins c. 1 km above a Devonian paleo-subduction interface, interpreted as metasomatized former felsic dyke networks crosscutting the mantle wedge peridotites. Here, both jadeitites and associated amphibole-rich dark granofels display widespread brittle-ductile deformation fabrics such as shear bands, foliated cataclasites and breccias, cemented through dissolution-precipitation processes by omphacite and sodic amphiboles, a mineral assemblage typical of high-pressure–low-temperature subduction zone conditions. Electron probe and laser ablation ICP-MS mapping indicate that these brittle-viscous networks display a substantial metasomatic imprint highlighted in the dark granofels by variations in major and trace elements. Switches between viscous and brittle deformation patterns are attested by crystallographic-preferred orientations of jadeite in some of the shear zones that crosscut the host jadeitites. Strikingly similar mineral assemblages and deformation patterns were observed in the Kashin and Motagua samples. Observed deformation features in these localities can be classified into three categories (tectonic breccias, foliated cataclasites and hydraulic breccias), which may occasionally form in sequence and exhibit mutually overprinting textures. Some of the foliated cataclasites contain fine-grained and foliated “shard-like” features forming a radial omphacite-jadeite spherulitic texture, interpreted as former pseudotachylyte that evokes a paleo-seismic origin. We interpret these healed fault networks as

48 recording external fluid influx within fracture zones that repeatedly ruptured along former "dyke"
49 networks. These high permeability drains likely (i) contribute to the transfer of highly pressurized plate-
50 interface metamorphic fluids into the mantle wedge; and (ii) trigger seismic instabilities recorded in the
51 basal part of active mantle wedge sections. These findings provide new insights into the current
52 understanding of the rheology (e.g., serpentinization ratio) and stress state in the mantle wedge, with
53 implications for subduction interface seismogenesis.

54 **1. Introduction**

55 Understanding processes rooted in the mantle wedge region of subduction zones is of critical
56 importance because its structure strongly controls the rheology of the subduction interface at the
57 downdip end of the seismogenic zone (Hyndman & Peacock, 2003; Dessa et al., 2009; Agard et al., 2018).
58 Fluids released by metamorphic reactions in the downgoing plate are thought to control the degree of
59 hydration (serpentinization) of the fore-arc mantle wedge (e.g., Hacker et al., 2003; Deschamps et al.,
60 2010; Bostock, 2013). The bulk serpentinization ratio of the mantle wedge, estimated based on the
61 perturbation of seismic wave velocities, is generally considered low (i.e., <20 vol.%; Abers et al., 2017)
62 except for specific subduction environments where it may reach up to 60 vol.% (e.g., Central Japan:
63 Hyndman & Peacock, 2003; Mariana margin: Hussong, 1981). The serpentinized mantle wedge has long
64 been considered as mostly aseismic due to the presence of weak minerals such as antigorite or talc that
65 are known to substantially reduce rock strength (e.g., Hilairet et al., 2007). Yet, insights gained from
66 detailed studies on the Sumatra 2004 (M_w = 9.1) and Maule 2010 (M_w = 8.8) mega-earthquakes have
67 shown that some of these exceptional rupture events may nucleate or propagate at the base of the "cold
68 nose" region (e.g., Dessa et al., 2009; Wang et al., 2020). This paradox raises important questions
69 regarding the rheology of the partly serpentinized mantle above the subduction interface. The report of
70 slow earthquakes near the seismogenic downdip end of several subduction megathrusts also changed
71 our vision regarding stress distribution along the deep interface (e.g., Fu & Freymuller, 2013; Frank et al.,

2015; Audet & Kim, 2016), with potential implications for mega-earthquake prediction (Obara & Kato, 2016; Bouchon et al., 2018). Whereas it is now accepted that fluids dramatically impact the mechanical stability of the deep serpentinized interface, very little *in situ* information is known about fluid-rock interaction processes or the feedback between upward transported fluids and seismicity (e.g., Angiboust et al., 2014; Locatelli et al., 2018).

Over the last decade, an increasing number of high-resolution seismological studies have identified the presence of seismicity nests in the partly serpentinized mantle wedge (e.g., Halpaap et al., 2019 and references therein). These events are generally interpreted as mechanically related to the influx of fluids or melts between 30 and 70 km depth (e.g., Davey & Ristau, 2011). A majority of the clusters identified in literature concentrates in the first 15 km above the plate interface (e.g., Greece: Halpaap et al., 2019; Japan: Nakajima & Uchida, 2018; New Zealand: Davey & Ristau, 2011; Central Chile: Wang et al., 2020; Colombia: Chang et al., 2019) along steeply-dipping, planar features commonly seen as "vent-like" structures, apparently channelizing plate-interface fluids towards the inner wedge. Normal, strike-slip and thrust focal mechanisms are reported for a large majority of these supra-slab earthquakes, with magnitudes generally spanning a range between 2 and 5 (e.g., Halpaap et al., 2019). The physics of the rupture and the nature of the material where these earthquakes are nested remain unknown. Moreover, the source and the composition of the fluids passing through these networks is also a matter of discussion since the precise location of hydrous mineral breakdown reactions strongly depends on the subduction thermal structure (e.g., Hermann et al., 2006; Syracuse et al., 2010).

Natural mantle wedge samples, despite their scarcity worldwide, represent a unique opportunity to shed light on these deep-seated processes (e.g., Kepezhinskas et al., 1995; Horn et al., 2020). Jadeitites are known to represent fossilized fluid pathways from the base of the hydrated mantle wedge (Harlow & Sorensen, 2005; Harlow et al., 2015). From this perspective, they may provide insights on the physical nature of supra-slab seismic events. However, primary structures from jadeitite-bearing

localities have been almost systematically overprinted during long-term subduction, extensive serpentinization and exhumation (e.g., Central America: Flores et al., 2015; Kawamoto et al., 2018; Myanmar: Shi et al., 2009a; Japan: Morishita et al., 2007). In the Polar Urals (Russia), the Pus'yerka locality exhibits a relatively undisturbed contact between a jadeitite "dyke" network and its ultramafic host (e.g., Meng et al., 2011; Angiboust et al., 2021), thus providing an opportunity to identify deformation processes rooted in these jadeitite bodies. Through a combined petrological, microstructural and geochemical investigation of Polar Urals samples, we provide new evidence for brittle-ductile switches in jadeitites (and associated amphibole-phlogopite granofels) microstructures. These structures are compared with those from samples of loose jadeitite boulders from Myanmar and Guatemala, settings where pristine structures are only exceptionally exposed (e.g., Sorensen et al., 2010). We then evaluate their potential meaning in terms of fluid pathways and the genesis of seismic instabilities in the basal region of active mantle wedges.

2. Geological setting

2.1 Pus'yerka jadeitite deposit (Polar Urals, Russia)

The Polar Urals belt formed during closure of the Uralian ocean by subduction and by the eastward burial of the European continental margin under an oceanic volcanic arc (e.g., Savelieva et al., 2002). In the Polar Urals, the Main Ural Thrust (MUT; **Fig.1a**) corresponds to a major crustal-scale shear zone with peridotites that were thrust over eclogitized continental crust (Marun-Keu complex; e.g., Udovkina, 1971; Dobretsov & Sobolev, 1984; Glodny et al., 2003). Rare ophiolitic, blueschist-facies mélange exposures are restricted to the base of the MUT (e.g., Kazak et al., 1976). Locally, the MUT has been subject to moderate reactivation as a detachment fault during exhumation (e.g., Sychev & Kulikova, 2012). In the Polar Urals,

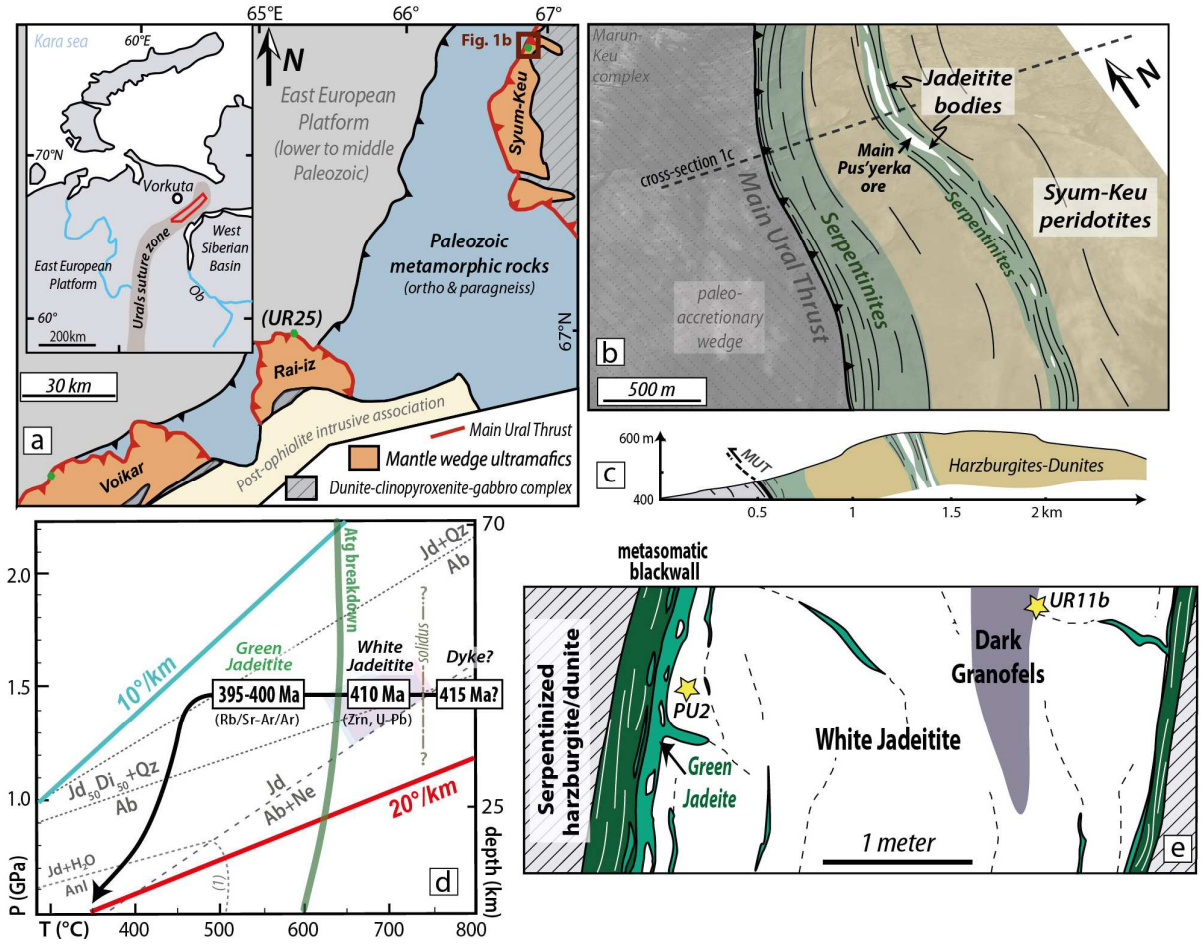

Figure 1. a. Simplified geological map of the Polar Urals locating the three main mantle wedge sections exposed in this region and the study area at the base of the Syum-Keu massif. The inset localizes the Polar Urals in northern Russia. Green dots correspond to jadeitite-bearing localities (modified after Angiboust et al., 2021). **b**. Geological map showing the structures above the Main Ural Thrust, interpreted as an ancient subduction interface. The studied jadeitite "dyke" crops out as a boudinaged sliver wrapped by a network of sheared serpentinites, approximately 1 km above the Main Ural Thrust. **c**. Cross-section highlighting the geometry of the structures identified in the field (modified after Angiboust et al., 2021). **d**. Pressure-Temperature-time sketch summarizing the long-term evolution of the Pus'yerka jadeitite dyke structure (after Angiboust et al., 2021). $Jd_{50}Di_{50}$ reaction line is after Maruyama & Liou (1988). Reaction (1): Analcime = Albite + Nepheline. **e**. Schematic view of the white jadeitite "dyke" as observed in situ in the Polar Urals with dismembered patches of dark granofels and dark amphibole-phlogopite bearing blackwalls forming at the contact with the host serpentinized ultramafic rocks. Mineral abbreviations after Whitney & Evans (2010).

three peridotite massifs (the Rai-Iz, Syum-Keu and Voikar massifs) were locally transformed into antigorite-schists along the MUT hangingwall (**Fig.1b**). These large mantle exposures, mostly harzburgitic and lherzolitic in composition (Savelieva & Suslov, 2014; Shmelev et al., 2011), exhibit large chromite deposits and are crosscut by numerous subvertical dunitic channels interpreted as the melt extraction pathways (Batanova et al., 2011). The MUT hanging wall displays (i) a serpentinization gradient towards the underlying unit; (ii) the presence of jadeite ($NaAlSi_2O_6$) veins in the serpentinites from the hanging wall; and (iii) a high pressure–low temperature (HP-LT) metamorphic imprint in the footwall units (e.g., Dobretsov & Ponomareva, 1968; Glodny et al., 2003; Batanova et al., 2011; Shmelev, 2011; Meng et al., 2016). The Rai-Iz, Syum-Keu and Voikar peridotite massifs in the Polar Urals can thus be viewed as good analogues of a supra-subduction setting, enabling the understanding of deep-seated processes below an inferred Paleozoic island arc (e.g., Batanova et al., 2011; Savelieva et al., 2002, 2016; Angiboust et al., 2021), in a region of the deep subduction interface that is not commonly exhumed (Guillot et al., 2009; Agard et al., 2018).

The studied Pus'yerka exposure is located along a jadeitite-bearing serpentinized shear zone that is several hundred meters thick and 5 km long, striking N-S and dipping E approximately 1 km above the Main Ural Thrust (MUT; **Fig.1b**). In a recent study, Angiboust et al. (2021) have interpreted the MUT hanging wall as a rare natural case study highlighting the structure along the base of a subduction mantle wedge. This major jadeitite deposit, discovered and mined in the 1980s (Kuznetsov et al., 1986; Fishman, 2006), represents a unique locality to investigate the structural contacts between the jadeite bodies and its host (e.g., Meng et al., 2011; Angiboust et al., 2021).

The basal serpentinites as well as the jadeitite-bearing network exhibit a regional foliation parallel with the MUT (**Fig.1c**). Field, geochemical and density measurements indicate serpentinization ratios in the range of 35-65 vol.% (in agreement with the 45-65 vol.% estimates from Makeyev, 1992), with up to

90-100% approaching the MUT and within the jadeite-bearing networks (**Fig.1b**; Angiboust et al., 2021 and references therein). The serpentinite schists that host the jadeitite boudins are composed of antigorite with minor amounts of brucite, magnetite and phlogopite (Makeyev, 1992) as well as chlorite, tremolite and magnesite. Within the serpentinite shear zone, tens of whitish jadeitite lenses are observed, elongated *en echelon* and stretched parallel to the main foliation dip direction (**Fig.1b**). The thickness of these lenses ranges between several tens of centimeters to several meters in the few places where the lenses were observed *in situ* (e.g., Kuznetsov et al., 1986; Meng et al., 2011).

Ion probe U-Pb dating of zircon crystals from the main jadeitite body yielded U-Pb ages of 404 ± 7 Ma (Meng et al., 2011) and 409 ± 3.3 Ma (Konovalov & Sergeev, 2015). These Devonian ages were interpreted by Meng et al. (2011) as dating intra-oceanic subduction initiation of the Uralian ocean realm. Angiboust et al. (2021) proposed that these jadeitite bodies derive from the metasomatic replacement of a former trondhjemitic dyke that crystallized from slab-derived melts within an ultramafic mantle wedge setting, in a subduction initiation context (i.e., at a temperature regime much higher than expected in a long-lived subduction context; e.g., Soret et al., 2016 and references therein). Ar-Ar plateau ages and multi-mineral Rb-Sr dating yield ages for phlogopite and amphibole-bearing domains ranging from 410–395 Ma, interpreted by Angiboust et al. (2021), in line with the pioneering study of Dobretsov & Ponomareva (1968), as marking the re-equilibration of dyke material during secular cooling from supra-solidus to HP-LT conditions (i.e., from T > 700°C to T < 500°C for a pressure on the order of 1.5 GPa). The studied samples were collected in the main jadeitite "dyke" (**Fig.1b,e**).

2.2 Kashin state Jade Mines Belt (northern Myanmar)

One of the world's largest jadeitite-bearing suture zones is exposed in the Kashin state of Myanmar in the famous Jade Mines Belt (e.g., Shi et al., 2012; Nyunt et al., 2017), where loose jadeitite fragments are found in conglomerates, river beds or exceptionally embedded within strongly-weathered

antigorite schists (e.g., Harlow et al., 2015 and references therein; Ridd et al., 2019). The original jadeitite-bearing structures (likely ancient felsic dykes; e.g., Bleeck, 1908) were formed within a serpentinized mantle wedge from a subduction zone of debated Late Jurassic to Late Cretaceous age (Goffé et al., 2002; Shi et al., 2009a, 2012; Yui et al., 2012; Harlow et al., 2015). These metasomatized dykes were extensively affected by exhumation and subsequent strike-slip deformation related to the Sagaing transform fault system (Harlow et al., 2015; Searle et al., 2017; Ridd et al., 2019). Protracted deformation led to the formation of a serpentinite mélange in which jadeitite "dykes" and blocks were disrupted and disseminated in the antigorite schist matrix, together with other lenses of seafloor origin such as graphite schists, glaucophane schists, garnet amphibolites and garnet micaschists (Nyunt et al., 2017).

Although the original thickness of the jadeitite "dykes" is challenging to evaluate due to poor exposure conditions and late deformation, some studies mention typical thicknesses on the order of several meters (Shi et al., 2012, Harlow et al., 2015 and references therein), in line with the structures observed *in situ* in the Polar Urals (**Fig.1e**). Texturally secondary chlorite schists ("blackwalls") as well as albitite bands are reported at the contact between the dyke structure and the host (Bleeck, 1908; Chhibber, 1934). Na-amphibole-rich bands (mostly eckermannite and glaucophane; see Oberti et al., 2015 for further details on mineralogy) are also found either embedded within the jadeitite "dyke" or lining the contact with the ultramafic host (Bleeck, 1908; Nyunt, 2009). Most pressure-temperature estimates for jadeitite formation in the Jade Mine Belt region span a wide range from 1.0–1.5 GPa and 300–500°C (Mével & Kiénast, 1986; Goffé et al., 2002; Shi et al., 2003). The herein studied samples, provided by a local miner, were found as boulders in a conglomerate near the Lonkin township (near Hpakan).

2.3 Motagua fault zone (Guatemala)

202 The Guatemala suture zone is an E-W-trending major plate boundary zone that separates the
203 Caribbean and North American plates. This strike-slip suture, which puts in contact the Maya block to the
204 north with the Chortis block to the south (e.g., Ortega-Gutierrez et al., 2007 and references therein),
205 contains many mafic and ultramafic blocks as well as eclogite-, blueschist- and garnet amphibolite-facies
206 crustal and sedimentary fragments interpreted as remnants from a Cretaceous meta-ophiolite (e.g.,
207 Brueckner et al., 2009). The Motagua fault zone separates two distinct terranes likely exhumed during
208 two distinct collisional events: the North Motagua and the South Motagua mélanges (e.g., Beccaluva et
209 al., 1995; Gendron et al., 2002; Harlow et al., 2004; Harlow, 2011). Different metamorphic ages on
210 jadeitites and eclogites were reported for these two terranes, ranging from c. 100–60 Ma for the North
211 Motagua and c. 160–110 Ma for the South Motagua mélanges (see Flores et al., 2013 and references
212 therein). The highest-pressure rocks from these two mélanges are also slightly different, with 500–650 °C
213 and 1.5–2.3 GPa for the North Motagua mélange (Harlow et al., 2008; Tsujimori et al., 2004) and 470–
214 520 °C and 2.0–2.7 GPa (Tsujimori et al., 2006; Endo et al., 2012) for the South Motagua mélange.

215 Jadeitites occur as meter-sized blocks within the serpentinite mélanges but are most commonly
216 found as pebbles within streams or as loose blocks in slope debris. As for the Jade Mines Belt in
217 Myanmar, pristine tectonic relationships are extremely difficult to document. The mineralogy of
218 jadeitites is quite varied in terms of minerals and mineral abundances, and with contrasting assemblages
219 in the north and south Motagua mélanges (Harlow et al., 2011; Flores et al., 2013). The herein studied
220 samples were collected as loose boulders in streams from the southern Motagua mélange (Rio El Tambor
221 area) and contain essentially jadeite plus minor omphacite and lawsonite, in agreement with the
222 mineralogy of jadeitites from this mélange (Harlow et al., 2011).

223 **3. Analytical methods**

224 *3.1 Electron probe microanalysis*

225 Mineral compositions were quantified via electron probe microanalysis (EPMA) using a Cameca
226 SXFive operated in the CAMPARIS analytical facility at Paris University. Standard analytical conditions (15
227 keV, 10 nA, beam diameter 5 µm) and a set of synthetic and natural crystals for calibration standards
228 were used: Fe_2O_3 (Fe), $MnTiO_3$ (Mn, Ti), diopside (Mg, Si), CaF_2 (F), orthoclase (Al, K), anorthite (Ca) and
229 albite (Na). X-ray maps were acquired on the same instrument using analytical conditions of 15 keV, 250
230 nA, a dwell time of 60 milliseconds and a step size of 2 µm. Some of the X-ray images were processed
231 and quantified with DWImager software (Torres-Roldán and Garcia-Casco, unpublished; see Garcia-
232 Casco, 2007). A scanning electron microscope (SEM) Zeiss EVO MA10 at the Institut de Physique du
233 Globe de Paris using internal calibration standards was used for microscopic investigations, energy
234 dispersive X-ray spectral (EDS) mapping and surface composition characterizations. Mineral
235 abbreviations are from Whitney & Evans (2010). Clinopyroxene and clinoamphibole compositions,
236 including estimation of Fe^{3+}, are calculated according to the schemes of Morimoto (1989) and
237 Hawthorne & Oberti (2007), respectively. Classification of these minerals also follows the same authors.

238 *3.2 Laser Ablation Inductively Coupled Plasma Mass Spectrometry*

239 Laser Ablation Inductively Coupled Plasma Mass Spectrometry (LA-ICP-MS) trace element maps
240 were acquired using a Resonetics M-50-LR 193 nm excimer laser coupled to an Agilent 7700x
241 Quadrupole ICP-MS housed at Adelaide Microscopy, University of Adelaide. Instrument conditions and
242 mapping protocols similar to that employed in this study are outlined in Raimondo et al. (2017). Pre-
243 ablation of each raster scan was completed to minimize the effect of redeposition (19 µm, 75% overlap),
244 followed by 15 s washout and 10 s of background measurement. A beam diameter of 19 µm, line spacing
245 of 19 µm and repetition rate of 10 Hz were employed for sample PU2, resulting in an energy density of
246 3.5 J/cm^2 at the target. Standards were analyzed in duplicate every 2 h during the mapping session,
247 including reference glasses NIST 610 (Pearce et al., 1997; Jochum et al., 2011a) and GSD-1D (Jochum et
248 al., 2011b). A beam diameter of 51 µm was used for all standard analyses, and included 5 pre-ablation

shots (51 µm, 75% overlap) followed by 20 s washout, 30 s background measurement and 40 s ablation time. Data acquisition was performed in time-resolved analysis mode as a single continuous experiment. Each analysis comprised a suite of 38 elements, and dwell times were as follows: 0.01 s (Li), 0.002 s (Na, Mg, Al, Si, K, Ca, Mn, Fe, Ni), 0.005 s (Sc, Ti, V, Cr, Nb, Ba, Hf, Th, U), and 0.008 s (Sr, Y, Zr, Ta, Pb, REEs). The total sweep time was 0.297 s. Post-acquisition processing was performed using the software Iolite (Woodhead et al. 2007; Hellstrom et al. 2008; Paton et al. 2011), with data reduction and image processing procedures following those outlined by Raimondo et al. (2017) and Hyppolito et al. (2018).

3.3 Electron Back-Scattered Diffraction and cathodoluminescence mapping

Electron Back Scattered Diffraction mapping (EBSD) has been performed at the Laboratoire de Géologie of the Ecole Normale Supérieure of Paris using a ZEISS SIGMA Field Emission Gun Scanning Electron Microscope equipped with an EDX (Energy Dispersive X-ray Spectroscopy; X-MAX) and an EBSD detector (Nordlys Nano, Oxford Instruments). An acceleration voltage of 15 keV, a beam current of 5 nA, an aperture of 120 µm, an inclination of 70°, an acquisition rate of 100 Hz, a working distance of 14 mm and a mapping step size of 2.8 µm were the analytical parameters chosen for the mapping. Data acquisition, post-processing treatment and statistical analysis were performed using Aztec, Channel 5 and MTEX software (Bachmann et al., 2010; Bachmann et al., 2011). For noise reduction, every single-pixel isolated data point was removed and followed by denoising MTEX procedures. Cathodoluminescence (CL) mosaic images were acquired using the Cathodyne (NEWTEC) device equipped with a motorized stage, a 12kV and 120 µA plasma, and 2 seconds of image acquisition time.

4. Field constraints on Polar Urals jadeitite body

In the Pus'yerka locality of the Polar Urals, the ore jadeitite body is mostly formed by a white jadeitite core that represents more than 90% of the "dyke" volume (see schematic dyke structure in **Fig.1e**). Locally, remnants of felsic lithologies (comprising an albitite groundmass with paragonite flakes

surrounded by a jadeite-bearing corona) were observed, suggesting that the white jadeitite formed by replacement of a leucocratic dyke (see the model in Angiboust et al., 2021; see also Dobretsov & Ponomareva, 1968 and Kuznetsov et al., 1986). The whitish jadeitite-rich domains comprise weakly to strongly foliated mafic blocks that host millimeter-sized intricate amphibole and phlogopite crystals (sample PU2). These domains, referred hereafter to as dark granofels (sample UR11b), were interpreted by Angiboust et al. (2021) to be produced by the influx of alkali-rich fluids in a warm mantle wedge environment, before the emplacement of the leucocratic dyke. Such amphibole-rich blocks occupying a similar structural position were reported in the Jade Mine Belt area (Myanmar) by Bleek (1908; see also Harlow et al., 2015).

The white jadeitite is transected by centimeter to decimeter-long cracks filled by phlogopite as well as dark-blueish amphibole-rich domains and emerald-green Cr-rich clinopyroxene (**Fig.2a, b**). While the bulk of the white jadeitite mass looks at a first sight microstructurally homogeneous, detailed observations highlight numerous locations where structures are brecciated, ranging from crackle- to mosaic-type breccias (e.g., Woodcock & Mort, 2008). Chaotic breccias, where substantial disruption of the original structure occurred, are also observed in jadeitites and associated dark granofels (**Fig.2b**). Lastly, centimeter- to decimeter-thick, strongly sheared phlogopite-rich metasomatic rinds are observed along the margins of the jadeitite body at the contact with the host serpentinite (**Fig.1e**; see also Kuznetsov et al., 1986 and Angiboust et al., 2021). Further south, directly below the Rai-Iz peridotite massif, occurs a tectonic mélange zone (“Nephrite brook”, Kazak, 1978; **Fig.1a**) that contains blocks of nephrite and rare jadeitite within a schistose serpentinite matrix. Sample UR25 represents one of these jadeitite pods, considered to be derived from a former “dyke” structure that has been fully disrupted by late subduction zone tectonic deformation.

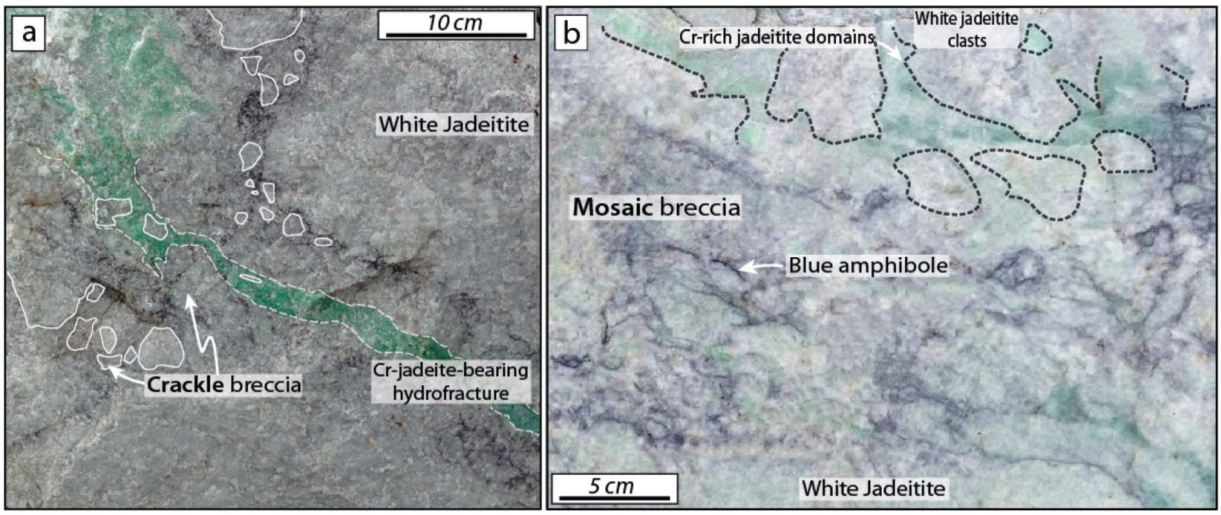

294

295 Figure 2. a. Field photo of a brecciated white jadeitite block, showing a discrete crackle breccia texture
296 transected by a hydrofracture filled with green Cr- rich jadeite. b. Field photo highlighting the structure of
297 a mosaic breccia, with disrupted white jadeitite fragments cemented by a Cr-rich jadeitic clinopyroxene.

298 The nomenclature used in **Table 1** is defined based on the following deformation criteria: Type (I)
299 corresponds to breccias formed by centimeter- to tens of centimeter-sized clasts exhibiting a substantial
300 shearing component, fracturing and size reduction through indentation processes. Such breccias can
301 typically reflect a damage zone deformation pattern. Type (II) brecciated materials are defined as a
302 highly localized fault zone with evidence of pervasive shearing, grain comminution and flow banding,
303 with pulverized wall clasts floating in a fine-grained matrix. Such microstructures are generally known in
304 the vicinity of fault cores and are hereafter termed "foliated cataclasites". Type (III) corresponds to
305 hydraulic breccias with millimeter to centimeter-sized clasts (which may have undergone rotation)
306 cemented by clinopyroxene or amphibole. Space-filling material can be either dendritic, oscillatory, or
307 strained.

308 **5. Structure of Polar Urals jadeitites**

309 The bulk of the white jadeitite matrix is formed by idiomorphic, oscillatory and intricate 100–500 µm-
310 long jadeite crystals (Meng et al., 2011). Their outer rims are commonly lined by Ca-rich, omphacitic

compositions as well as interstitial phlogopitic micas (Angiboust et al., 2021; **Fig.S1**; **Table 1** and **Table S1**). Despite an apparently homogeneous macroscopic texture, detailed petrographic investigations reveal that jadeite crystals exhibit widespread fracturing, dissolution and replacement textures (**Fig.3a,b**). Vein systems that range in color from white (jadeite composition) to green (Cr-rich jadeite or Cr-rich omphacite; **Fig.2a**) are ubiquitously found crosscutting the host jadeitite matrix (see also Franz et al, 2014). These veins are filled by idiomorphic to fibrous clinopyroxene crystals with locally oscillatory and/or dendritic textures (Kuznetsov et al., 1986; sample UR03b in Angiboust et al., 2021: Type III). Clinopyroxene crystals from brecciated samples exhibit clear evidence for pressure-solution (as shown by indentation and truncation textures), as well as solution-precipitation with fracture healing and overgrowth by a new (generally more omphacitic) clinopyroxene composition (**Fig.3a,b; Fig. S2**).

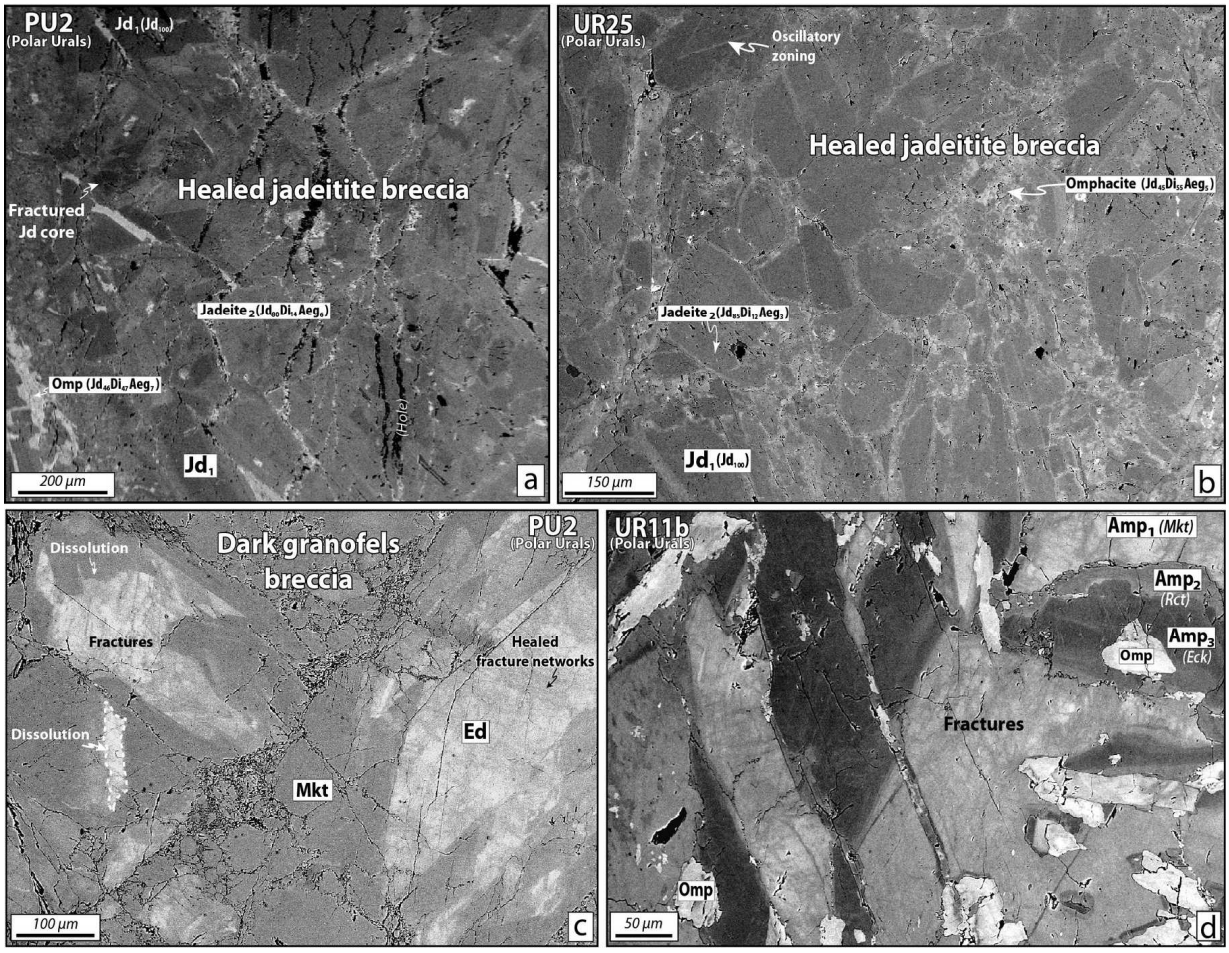

Figure 3. Backscattered electron (BSE) images for Polar Urals samples. a. White jadeitite specimen (PU2) showing highly disrupted clasts with evidence for fracturing, dissolution, indentation and re-precipitation. Several clinopyroxene generations can be identified with increasing diopside component towards clast rim. b. Example of a cryptic jadeitite breccia showing extensive fracturing, comminution and dissolution of dark white jadeitite clasts (locally exhibiting oscillatory zoning pattern). Location of sample UR25 given in figure 1a. c. Dark, amphibole-rich granofels that is heavily brecciated, with similar dissolution-reprecipitation features as well as extensive healed microfractures (sample PU2). d. Fractures associated with the growth of several amphibole compositions such as richterite (Rct) and eckermannite (Eck) overgrowing magnesio-katophorite (Mkt). Note that omphacite grows lately within a crack in textural equilibrium with Rct and Eck (sample UR11b).

The studied white jadeitite sample UR03d exhibits coarse-grained, idiomorphic and sector-zoned jadeite crystals in its matrix (**Fig.4a**). These crystals, generally extremely rich in jadeitic molecule (>90 mol.%), are hereafter referred to as Jd_1. The jadeite growth structures document how early structures have been transected by a localized fine-grained shear zone of oriented jadeite crystals with interstitial omphacite-rich grains. Orientation maps (**Fig.4b**) show that [001] axes are dominant along the fine-grained shear zone, whereas [100] and [010] axes become important approaching the margins of the shear band. Intracrystalline misorientation EBSD maps, depicting misorientation angles between each data point and the mean orientation of the parent crystal (**Fig. S3**), show that grains at the shear zone margins are highly misoriented. In addition, the finer grains within the shear band are consistently devoid of intragranular misorientation except for strongly misoriented larger grains.

We interpret that the strongly misoriented clasts may represent fragmented remnants affected by brittle localized shear followed by dynamic recrystallization, resulting in the ubiquitous lack of misorientation in the surrounding finer-grained material. This pattern is highlighted by microscopic observations and strong crystallographic-preferred orientation (CPO), with [001] axes maxima but also forming a weak girdle along the stretching lineation and the foliation plane, respectively, whereas [010] and [100] display

maxima subperpendicular to it (normal to and within the foliation plane, respectively; **Fig.4c**). This fabric, similar SL-type tectonites, is reported in many previous omphacite (a mineral rheologically similar to jadeite and diopside) fabrics in eclogites (e.g., Philippot & Van Roermund, 1992; Godard & Van Roermund, 1995; Keppler et al., 2016), compatible with near-plain strain dislocation creep deformation mechanisms (e.g., Zhang et al., 2006; see also the review paper from Keppler, 2018). In addition, truncation of oscillatory zoning in jadeite crystals from the shear band denotes the contribution of solution-precipitation mechanisms. Thus, the fabrics herein observed indicate that a large part of the material involved in the shear zone (in particular the dark-shaded, fine-grained jadeite rims visible in **Figure 4a**) grew syn-kinematically, most likely via crystal-plastic deformation processes coupled with dissolution-precipitation creep.

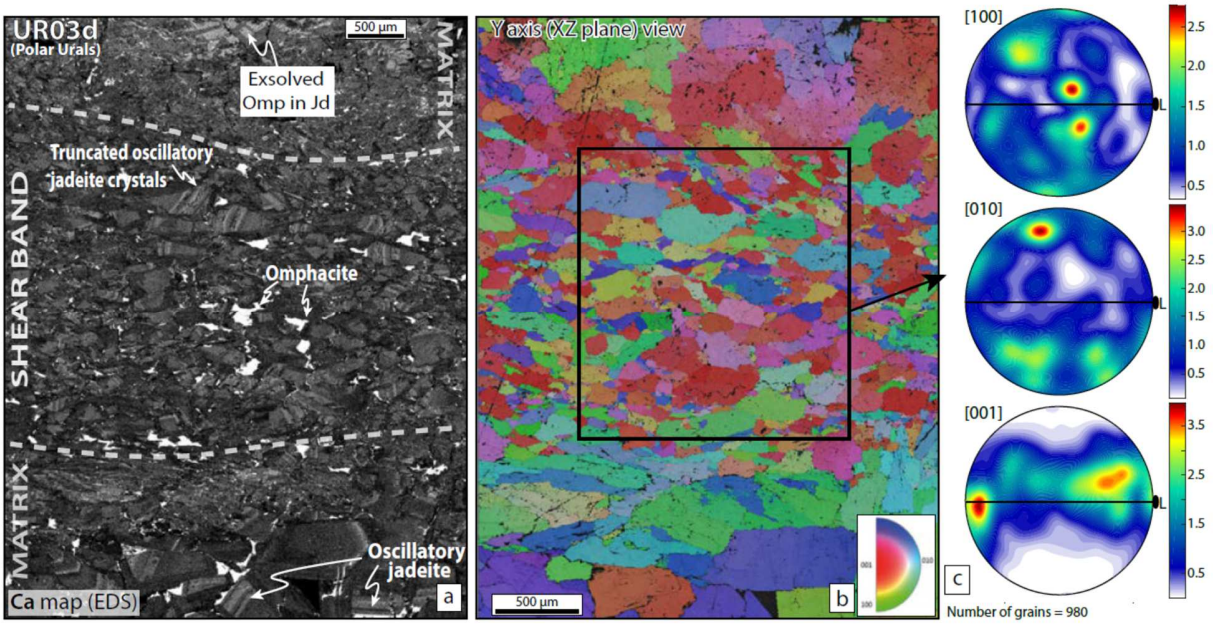

Figure 4. a. EDS X-ray map (counts of Ca, brighter shades indicating greater elemental concentrations) showing the structure of a shear band that transects a white jadeitite sample (PU3) from the Pus'yerka deposit. The coarse-grained oscillatory white Jd_1 crystals are deformed within the shear band into oriented and truncated aggregates of jadeite crystals with local omphacite overgrowths. **b**. EBSD orientation map colored according to the inverse pole figure key (IPF) of jadeite (bottom right), showing a shape preferred orientation to the X direction of the strain ellipsoid (i.e., stretching orientation). View (XZ

plane) corresponding to the Y axis of the finite strain ellipsoid. **c**. Pole diagrams of jadeite from the shear band (black square in panel b) represented in an upper hemisphere equal-area projection for [100], [010] and [001] crystallographic axes. Contours are multiples of uniform density distributions. The bold dot on the L axis represents the stretching lineation direction (X direction of the strain ellipsoid), and the black line represents the foliation plane.

6. Texture and mineral chemistry of Polar Urals dark granofels

The dark granofels found within and along the white jadeitite "dykes" from the Pus'yerka locality exhibits striking evidence for ductile and brittle shearing. Coarse idiomorphic calcic to sodic-calcic amphibole cores of edenite ($NaCa_2Mg_5Si_7AlO_{22}(OH)_2$) to Mg-katophorite ($Na(CaNa)Mg_4AlSi_7AlO_{22}(OH)_2$; *Amp*$_1$ brighter Ca-rich cores in BSE imaging mode) form a dense network of dark, sealed fractures as well as indentation and dissolution-precipitation features (**Fig.3c,d**). Various mutually overgrowing generations of amphiboles ranging from Mg-katophorite (*Amp*$_2$ on **Fig.3d**) to sodic amphiboles such as eckermannite ($NaNa_2(Mg_4Al)Si_8O_{22}(OH)_2$; *Amp*$_3$) or richterite ($Na(CaNa)(Mg,Fe)_5Si_8O_{22}(OH)_2$) fill the breccia inter-clast space in apparent textural equilibrium with omphacite (see also Angiboust et al., 2021). In sample PU2, a dark granofels layer is observed (adjacent to a micro-fractured white jadeitite domain), containing oriented sodic-calcic amphibole-phlogopite (± omphacite ± clinochlore) crystals (**Fig.5a**). Pervasive grain size reduction occurred through micro-brecciation (**Fig.5b,c,d**) followed by further comminution that ultimately led to the formation of anastomosing foliated cataclasite networks (**Fig.5e,f,g**; Type II). During (or after) grain size reduction, the large primary amphibole porphyroclasts of edenitic to magnesio-katophoritic compositions (with irregular Cr enrichments; **Fig.5c,g**) were re-equilibrated along their rims and fractures with very fine-grained pulverized domains with richteritic to eckermannitic compositions (**Fig.5c,f**). It thus appears that fracturing and milling occurred after (or during) the formation of Mg-katophorite around the edenitic rims. LA-ICP-MS trace element mapping shows that the Mg-katophorite clasts are enriched in Cr, Nd, Zr and Y, whereas the fine richterite-eckermannite intergrowths are relatively enriched in Li and Ni (see **Fig. S4**).

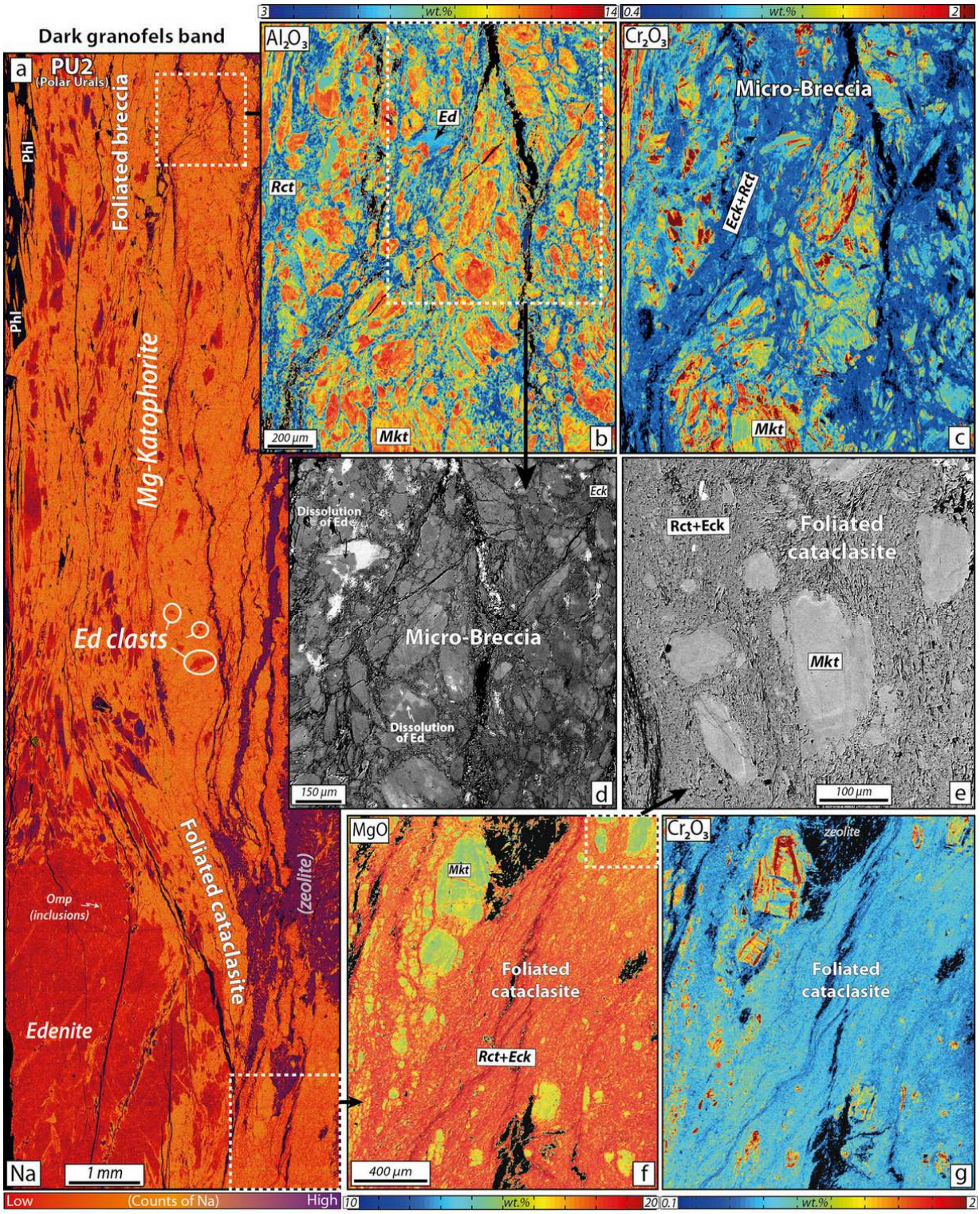

Figure 5. a. EDS X-ray map (counts of Na) showing the internal structure of a shear band crosscutting a dark granofels (sample PU2, Polar Urals). Primary edenite compositions (large clast) are gradually transformed along their rims into Mg-katophorite to richteritic compositions. Remnants of the original

edenite clasts are found floating in the Mg-rich domain, associated with oriented phlogopite (Phl) as well as rare omphacite and clinochlore crystals. **b** and **c**. EPMA X-ray maps showing a close-up on the foliated, matrix-rich, clast-supported chaotic breccia. **d.** BSE image showing dissolution features of the primary edenitic amphibole. **e**. BSE image showing a region of the shear band exhibiting a typical foliated cataclasite texture with Mg-katophorite clasts wrapped in a richterite+eckermannite fine-grained matrix. **f** and **g**. EPMA X-ray maps showing the internal structure of the foliated cataclasite as well as the presence of pre-fracturing Cr sector zoning in Mg-katophorite crystals. Some trace element maps for this sample are provided in **Fig. S4**. Texturally late Na- and Ca-rich zeolites grow as patches and along fractures parallel with the main foliation.

An example of Type I mosaic breccia can be seen in **Fig. 6a** (sample UR11b), where clasts of Mg-katophoritic composition were also heavily affected by multiple fracturing events. Remnants from the most pristine amphiboles lie along the edenite-Mg-katophorite transition (see **Table S1** and **Fig. S4** for chemical properties). Omphacitic clinopyroxene is very common as inclusions within clast cores as well as along sealed fractures (**Fig.6d**). Several generations of Mg-katophorite (with the younger exhibiting increasing Na(B) and decreasing Ca contents; **Fig.6c**) can be identified within and around the clasts. Texturally late eckermannite crystals (together with nyboïte: $NaNa_2(Mg_3Al_2)Si_7AlO_{22}(OH)_2$) are found filling the clast's cracks as well as replacing quadrangular inclusions in the cores of the fragments (**Fig.6b**; see Angiboust et al., 2021 for details on mineral chemistry). The inter-clast space is filled with fine-grained Mg-katophorite fragments that coexist with zoned clinopyroxene (ranging from jadeite to omphacite in composition; **Fig.6d**) as well as micrometer- to tens of micrometer-sized chromian spinel crystals (surrounded by Cr-clinopyroxene; **Fig.6b; Fig. S2**). Electron probe mapping demonstrates that the inter-clast domain is relatively enriched in Al, Na, Ca and Cr with respect to the Mg-katophorite clasts (**Fig. S5**).

LA-ICP-MS trace element mapping of the brecciated region from the dark granofels (UR11b) shows Mg-katophorite cores exhibiting Cr oscillations equivalent to sample PU2 (**Fig.5g**), revealing cryptic fractures healed with amphiboles substantially enriched in Zr, Hf, Y, Cr, Li and Ba (**Fig.6e,f,g; Fig. S5**).

Similar enrichments are distinguished within clinopyroxene-rich fracture-fill material (**Fig. S5**). Patchy enrichment in Li, Ba, Sr, Y and Ce (among other elements) is also visible in the amphibole-clinopyroxene inter-clast domain (see **Fig. S5** for further maps as well as normalized trace-element spider diagrams).

Figure 6. **a.** EDS X-ray map (counts of Al, brighter shades indicating greater elemental concentrations) depicting the chaotic breccia texture with the various healed fracture networks, as well as the location of both LA-ICP-MS and electron probe maps (sample UR11b, Polar Urals). **b**. EPMA-based masked phase map showing the various Mg-katophorite generations (green), eckermannite (blue) and nyboïte (violet). Omphacite is in light yellow shades, jadeite in deep orange and chromite (Chr) in red. Note how the various fracture generations are mutually overprinting. **c**. Amphibole masked map showing the Na(B) content. Increasing Na(B) is commonly viewed as reflecting a decreasing P/T ratio (closer to HP-LT conditions). **d**. Masked map of Na content in clinopyroxene showing two distinct compositions in the breccia-filling material. **e, f** and **g**. LA-ICP-MS masked trace element maps (amphiboles only) showing Y, Zr and Cr concentrations (in ppm). The full analytical dataset is given in **Fig. S5**. Black arrows indicate Zr and Y enrichments in the healed fractures and in the inter-clast matrix.

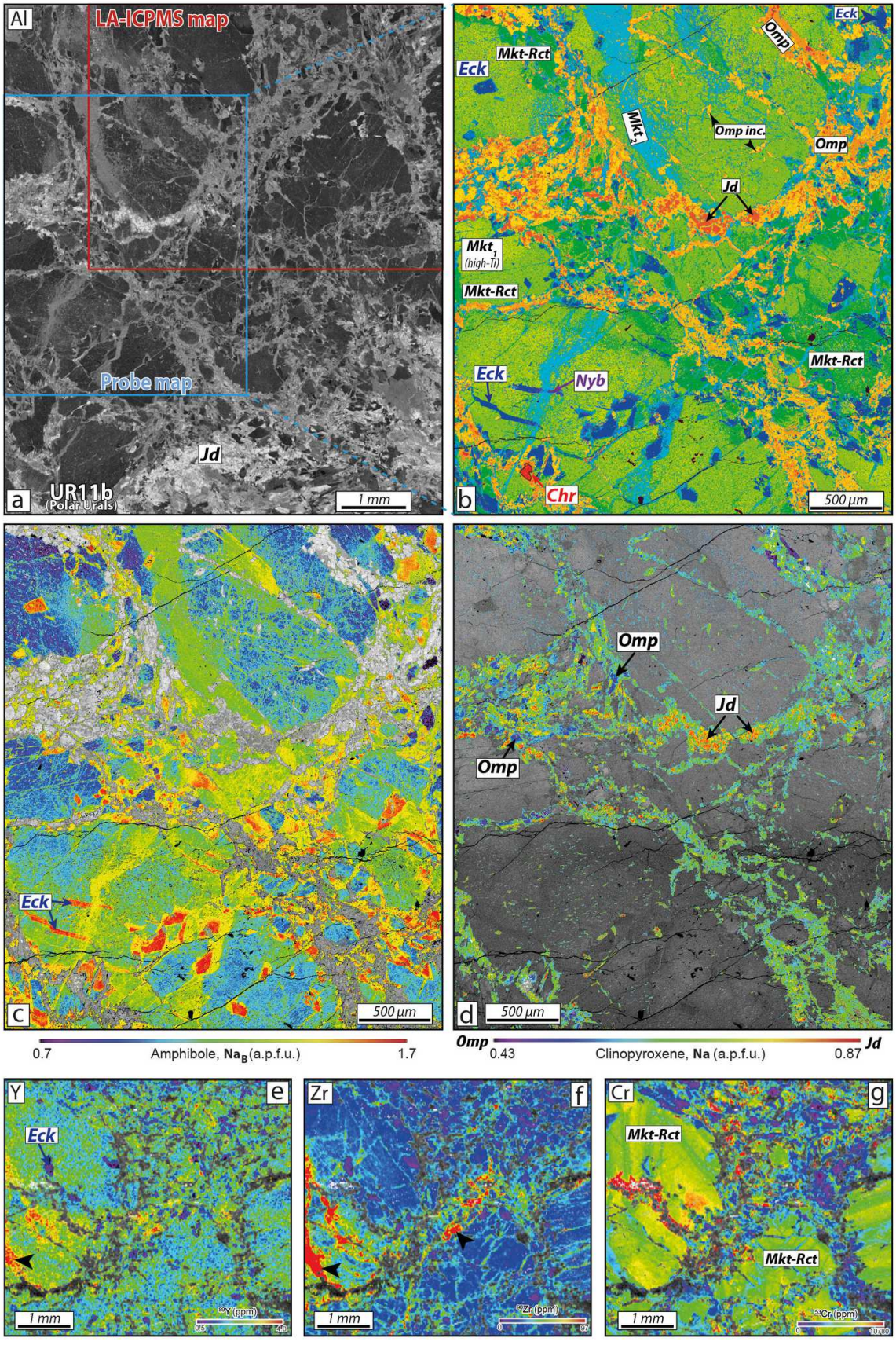
Al
LA-ICPMS map
Probe map
Jd
a
UR11b
(Polar Urals)
1 mm
Eck
Mkt-Rct
Omp
Mkt2
Omp inc.
Jd
Mkt1
(high-Ti)
Nyb
Chr
b
500 µm
c
d
0.7
Amphibole, NaB (a.p.f.u.)
1.7
Omp
0.43
Clinopyroxene, Na (a.p.f.u.)
0.87
Jd
Y
e
Zr
f
Cr
g

7. Deformation and mineral chemistry of Motagua (Guatemala) jadeitite breccias

Macroscopic evidence for brecciation of the Motagua region jadeitites is widespread in the studied samples (see also Harlow, 2011 and references therein). Three types of deformation patterns were observed: (i) deep green fractures crosscutting white jadeitites (Type I, **Fig.7a,b**); (ii) finely comminuted foliated breccia and cataclastic patterns (Type II, **Fig.7e**); and (iii) hydraulic-like breccias where millimeter- to centimeter-sized angular clasts are infiltrated by a fibrous, oriented jadeitite (bluish) cement (Type III, **Fig.7c,d;** see below). Whereas the clasts forming the breccias are systematically whitish to light-greenish along their rims, the fracture- and breccia-filling material is always darker, ranging from dark green (**Fig.7a,b**) to deep blue (**Fig.7c,d,e**). The inter-clast domain filling these breccias is always enriched in Ca, Mg and Fe and depleted in Na and Al, as a consequence of omphacite growth. The replacement of the original jadeite (Jd_1, of near pure jadeite composition) by a secondary clinopyroxene (Jd_2, commonly slightly poorer in jadeite molecule ($80 < Jd_2 < 90$ mol.%) and *Omp*) is pervasive, affecting the entire breccia and not only the clast margins (**Fig.8a,b**). Fracture-filling clinopyroxene exhibits feather-like omphacitic crystals (**Fig. S2**) as well as a texturally strained appearance (**Fig.8a**). The Mg EDS map in **Fig.8a** shows relict white jadeitite clast cores (also visible on the hand specimen image in **Fig.7e**) affected by pervasive re-equilibration (dissolution-precipitation) by Ca-rich jadeite and omphacite compositions along crystal joints, fractures, grain boundaries and micro-faults.

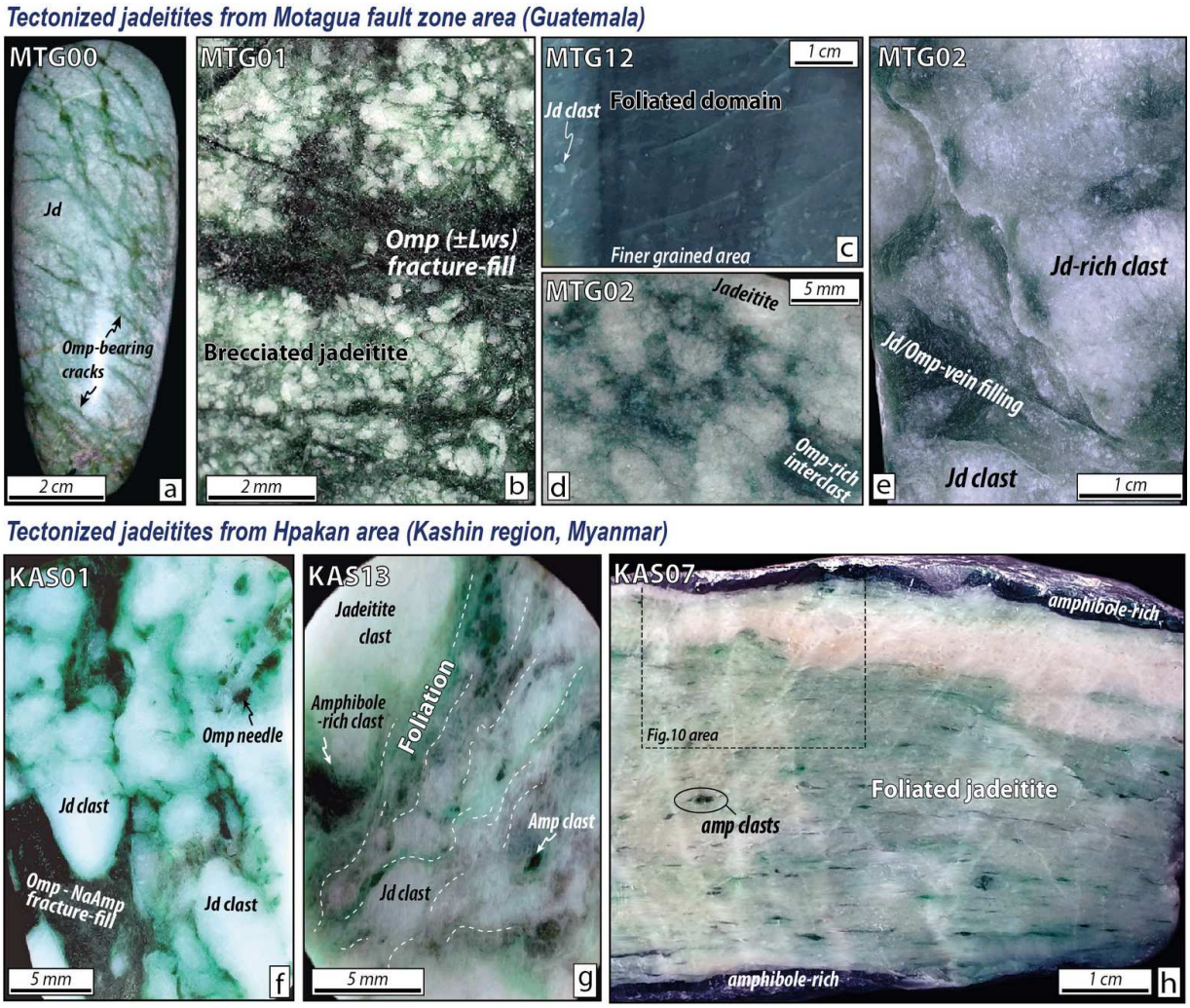

456

457 **Figure 7. a**. Polished axe carved in a Motagua fault zone jadeitite. This artefact has been found in El Manati
458 excavation (Olmec civilization, 2500–500 B.C; Veracruz state, Mexico; length: 105 mm, weight 189.5 g,
459 density 3.24). It shows numerous omphacite-bearing fractures characteristic of a nearby fault zone system
460 (Type I). Courtesy of F. Gendron (MNHN, Paris). **b**. Polished rock slab showing numerous white jadeitite
461 domains rimmed by a dark-green omphacitic clinopyroxene. This sample is cut by a fracture that exhibits
462 fibrous omphacite crystals as well as rare lawsonite crystals. **c**. Type II jadeitite sample showing the host
463 that is transected by a foliated domain comprising white jadeitite clasts. **d**. Jadeitite breccia (Type III) with
464 clasts fractured and healed by a blueish omphacite. **e**. Jadeitite breccia (Type III) with clasts pervasively
465 fractured and partly recrystallized along their rims by a secondary, greyish jadeite composition, and later
466 cemented by a deep blue ('Olmec') jadeite composition. **f**. White jadeitite clasts forming a breccia texture
467 with Cr-enrichments along their rims and cemented by fibrous sodic clinopyroxenes (Type III). **g**.
468 Moderately foliated breccia showing intermixed dark amphibole-rich clasts and white jadeitite clasts. **h**.

Strongly foliated white jadeitite matrix in between two foliated dark granofels bands (Type II). Note the large amount of blue amphibole clasts wrapped in the main clear foliation. The white boudin corresponds to a remnant of the pre-deformation pure jadeitite (Jd_1).

In Type II fault rocks, a centimeter-thick layering with variable shades of blue-grey (**Fig.7c**) is observed transecting the original white jadeitite (**Fig.9a**). Pale, clast-like patches (of pure jadeite composition) are macroscopically visible both in the host jadeitite as well as within the deep blue layers (see **Table S1** for representative mineral compositions). Microscopically, the bands are composed of very fine-grained (5–15 μm on average diameter) jadeitite fragments cemented by omphacite-rich compositions in interstitial positions (**Fig.9b,c,d,g**). Interestingly, this apparently pulverized domain also hosts "shard-like" features ranging in size from several tens to hundreds of microns (**Fig. 9e,f,g**). These shards (locally showing ptygmatic folds and contortion) define a weak lamination, resembling the "fiamme" textures known in ignimbrites and other pyroclastic flow deposits. Many of these shards display a fibro-radial intergrowth of jadeite and omphacite fibers that evoke the textures reported in spherulites formed after the devitrification of a former glass (**Fig.9g**). SEM-based surface estimates of these shards yield compositions ranging between those measured for jadeite and omphacite crystals (**Fig.9c,h**). The shard-bearing fault zone domain shown in **Fig.9b** is transected by a dark, very fine-grained omphacitite band that seems connected with the network of omphacite-bearing hydrofractures that transect the rock volume. Remnants from foliated fragments of the host (namely the white jadeitite Jd_1 but also the foliated shard-bearing domain) are observed, strongly dissolved, within this omphacitite band. A metasomatic reaction front also appears to have formed at the contact between these two domains (**Fig.9b**).

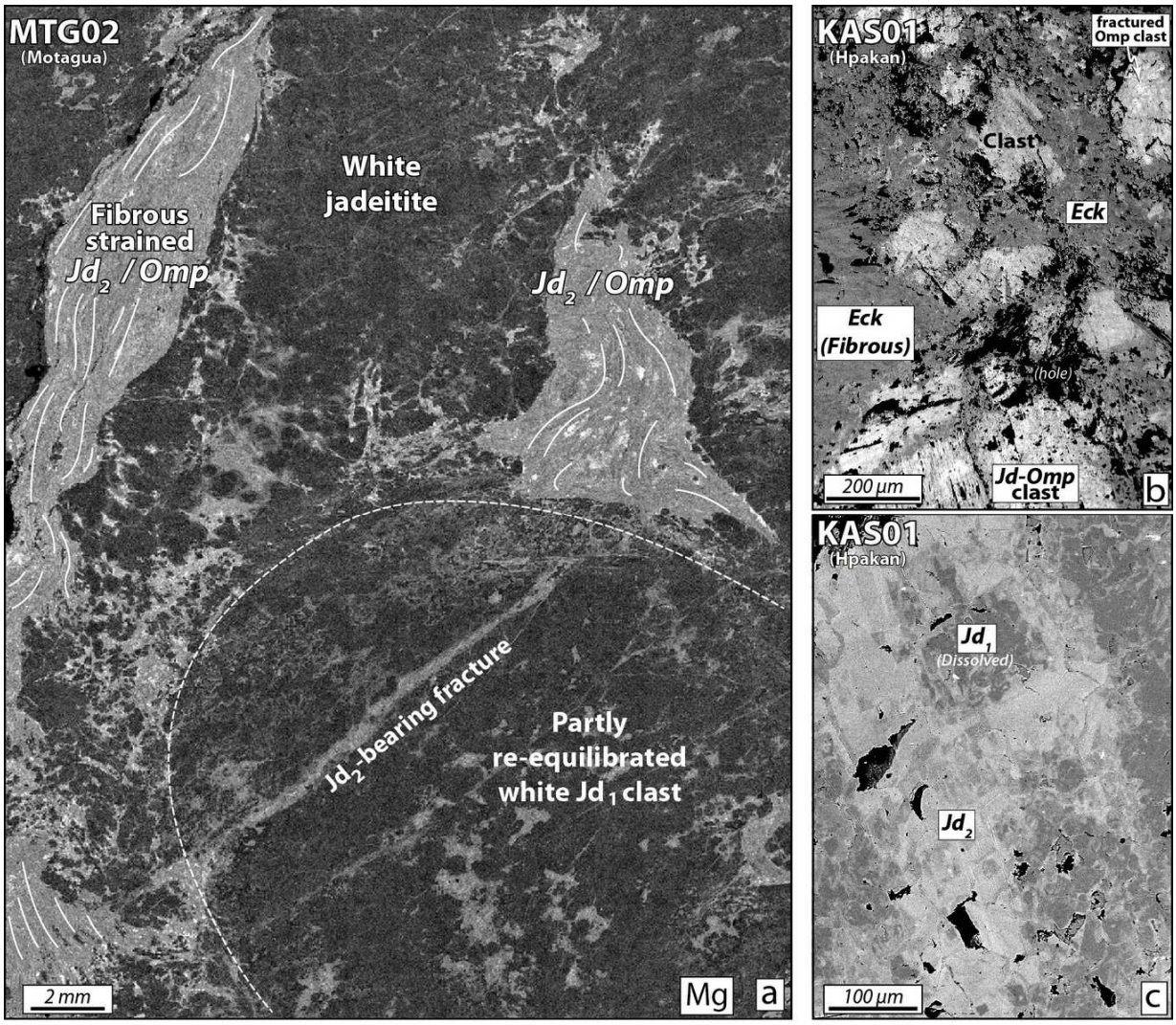

490

491 **Figure 8. a.** EDS X-ray map (counts of Mg, brighter shades indicating greater elemental concentrations)
492 depicting a Type III hydraulic breccia texture with fibrous clinopyroxene fills (see **Fig. S2** for further images;
493 Motagua region, Guatemala). Note how the Jd_1 clasts are corroded and replaced by a secondary jadeite
494 (richer in omphacitic component) along grain boundaries, micro-fractures as well as inside the clasts. **b**.
495 BSE image of a brecciated jadeitite with fibrous eckermannite (sodic amphibole) infills (Myanmar). **c**. BSE
496 image showing dissolved primary Jd_1 generation (nearly Jd_{100}) replaced by a secondary Jd_2 composition
497 (slightly more enriched in omphacite).

498

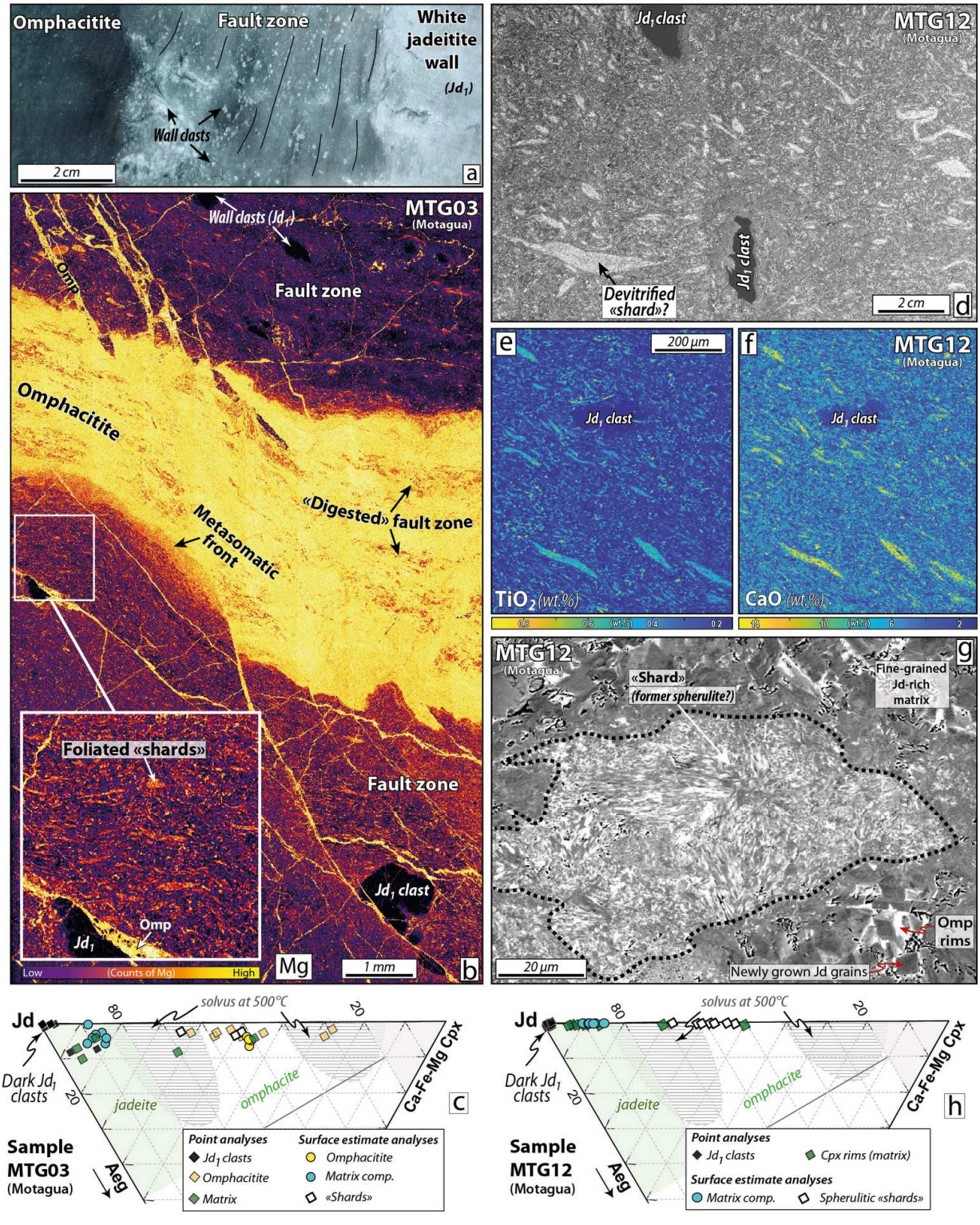

499

500 **Figure 9. a.** Hand specimen image of a Motagua jadeitite showing deformation features of the pristine
501 white jadeitite on the right, the foliated clast-bearing domain in the center (Type II texture) and a

secondary omphacitite band on the left. **b**. EDS X-ray map (counts of Mg) depicting a Type II matrix hosting white jadeitite clasts (in black), foliated "shards" as well as late omphacite-bearing hydrofracture networks. **c**. Clinopyroxene composition in the Jd-Di-Aeg triangle (after Morimoto, 1989; MTG03). Solvus domains for clinopyroxene are derived from Garcia-Casco et al. (2009). **d**. BSE image showing the typical appearance of a Type II foliated cataclasite matrix where shards and partly re-equilibrated white jadeitite clasts coexist. Note how the shards are randomly folded but yet define a mild foliation. **e** and **f**. Quantified EPMA X-ray maps of TiO_2 and CaO contents (in wt.%) showing elemental distributions in a clast and shard-bearing, Type II foliated cataclastic matrix. **g**. High-magnification BSE image showing a shard that exhibits a fibro-radial internal structure that evokes devitrification spherulites. Note how the finely-comminuted clasts forming the pulverized matrix were overgrown by a new (locally facetted) omphacitic clinopyroxene composition during fault consolidation and fluid-enhanced sealing. **h**. Clinopyroxene composition in the Jd-Di-Aeg triangle (sample MTG12). Note how shards are systematically enriched in omphacitic content.

8. Deformation and mineral chemistry of Hpakan (Myanmar) jadeitite breccias

Further evidence for brecciation of jadeitites can be obtained observing the hand specimens from Myanmar shown in **Figs 7f, 7g and 7h**. These samples exhibit the most complex sequence of mutually crosscutting brittle events (**Table 1**). In **Fig.7f**, white (and slightly rounded) jadeitite clasts are rimmed by omphacite (light green domains) and wrapped by dark blue amphibole (eckermannite)-clinopyroxene intergrowths (**Fig.8b**). The pristine jadeitic pyroxene composition (Jd_1) is only preserved as islands in the middle of a brighter (in BSE) more omphacitic pyroxene (Jd_2 and Omp; **Fig.8c**). In sample KAS10, dissolved cores exhibiting exsolution features can also be observed, with two pyroxenes forming at the expense of a former one (**Fig. S2**). Jd_1 seems to have been replaced along grain boundaries by a fluid that triggered pervasive re-equilibration (mixed Type I and Type III deformation). In other samples, the same meso-scale structure exhibits a weak, omphacite-rich foliation wrapping remnants of the white jadeitite and dismembered amphibole-rich fragments (**Fig.7g**). This texture suggests that viscous flow may occasionally overprint previously formed brittle (Type I) brecciated zones.

Sample KAS07 displays a whitish, foliated band separating two dark granofels domains (**Fig.7h**). The leucocratic band comprises small, flattened dark amphibole fragments oriented parallel with the main

foliation (**Fig.10a**), as well as green trails characteristic of Cr-bearing omphacitic clinopyroxenes. A cathodoluminescence image (**Fig.10b**) of the whitish domain reveals the presence of three distinct jadeite-forming events in a Type II pattern deformation zone. The first is a green-colored aggregate (*Jd_1;* white jadeite: $Jd_{91}Quad_5Aeg_4$ on average) wrapped within a pink-colored foliated band (mostly *Jd_2*) that hosts numerous angular, green-shaded fragments clearly derived from the green *Jd_1* aggregate on the left of the image (**Fig.10b**). These green clasts range in size from several tens to hundreds of microns, and display widespread evidence of fracturing, dissolution and re-precipitation/overgrowth by a brighter, slightly more omphacitic composition (see for example **Fig.10c**; $Jd_{84}Quad_6Aeg_{10}$ on average). This fabric evokes a deformation by micro-fracturing, with substantial comminution accompanied with shearing and flow banding of the pink cataclastic domain.

In the same sample, an eckermannite-filled extensional vein (Type III) is observed crosscutting at low angles the foliated cataclastic domain (**Fig. S2**). A late pure jadeite formation event (*Jd_3*, in purple on **Fig.10b**) also occurs as foliation parallel bands, as patchy domains in the green-colored *Jd_1 augen* on the left of the image, as well as filling late cracks that crosscut all previous features. Sheared amphibole fragments (mostly eckermannite) appear dark in the cathodoluminescence image in the main foliated area (**Fig.10b**). BSE imaging and composition analysis reveal that the amphibole-rich band from the left part of this thin section (**Fig.10a**) locally contains Mg-katophorite cores rimmed by eckermannite or nyboïte compositions (see **Table S1** for representative mineral compositions). This brecciated amphibole-rich domain (likely a former Type I) has been cemented by a clinopyroxene-Na-amphibole mixture and foliated parallel to the adjacent foliated cataclasite domain (**Fig.7h, 10b**). A striking feature of this dark domain is the systematic decrease of Ca content in amphibole from the cores (Mg-katophorite; 7 wt.% CaO) to the foliated matrix, where amphiboles are extremely enriched in Na_2O (>11 wt.%) and depleted in CaO (<1.5 wt.%). Similar observations were made in sample KAS06 where cores are edenitic (up to 10

552 wt.% CaO), whereas crystals lining the foliation correspond to eckermannite, also closely associated with

553 strained jadeite crystals (see **Fig. S2** for EDS mapping and further details on mineral chemistry).

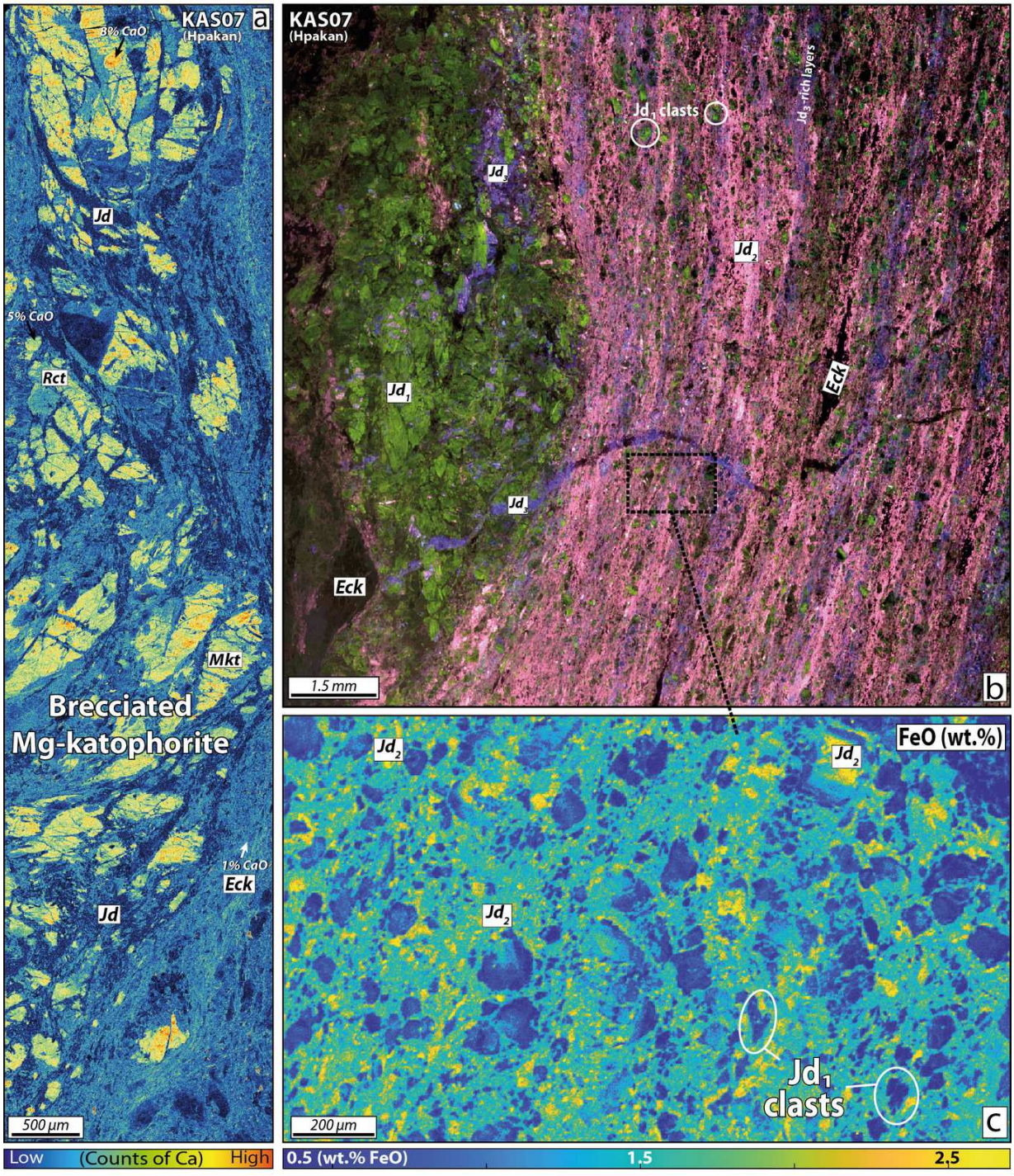

554

555 Figure 10. a. EDS X-ray map (counts of Ca) showing the internal structure of a foliated and brecciated dark
556 granofels layer with Mg-katophorite cores (locally containing up to 8 wt.% CaO) wrapped within a jadeite-
557 eckermannite-bearing foliation. b. Cathodoluminescence image of the whitish, foliated part of sample
558 KAS07. Note the white jadeitite (Jd_1; CL-colored in green) fragments now dispersed in the Type II foliated
559 cataclasite matrix (Jd_2; CL-colored in pink) and the black trails parallel with the foliation that are mostly
560 made of sodic amphibole (e.g., eckermannite). Late Cr-rich jadeite (Jd_3; CL-colored in purple) is also
561 observed parallel with the main foliation as well as along cracks. c. EPMA X-ray map showing FeO
562 distribution in the whitish foliated cataclastic domain. Note the random (Fe-poor) Jd_1 clast size distribution
563 as well as the apparent absence of internal deformation (such as plasticity) of Jd_1 clasts.

564 The most compelling evidence pointing to repeated brittle deformation events is exhibited in
565 **Fig.11** (sample KAS04). Three chemically distinct domains can be distinguished: (i) the white jadeitite
566 clasts (likely a former Type I structure); (ii) the blue amphibole fibrous veins that "inject" between
567 breccia clasts (e.g., hydrofracture-filling material); and (iii) a very fine-grained, greenish Type II foliated
568 omphacitite domain at the top of the sample (**Fig.11a**, **Fig.12f**). Locally, the contact between the blue
569 amphibole domains and the white clasts exhibits structures that evoke Type III hydrofracturing processes
570 (with local embayments pointing to interface-coupled dissolution-precipitation mechanisms; **Fig.11b**;
571 e.g., Putnis & Austrheim, 2013). A large surface of the same sample (KAS04) has been mapped using EDS
572 (**Fig.11c**) in order to image millimeter-scale relationships between these three domains. The largest
573 rounded, Al-rich white jadeite clast (colored in red) is transected along its base by a sharp micro-fault
574 plane, along which the green, very fine-grained material ("foliated cataclasite") is found. The green
575 omphacitite domain is formed by tens of micrometer-sized crystals (**Fig.11d**) that commonly contain dark
576 clasts (in BSE mode) with a composition similar to the large white jadeitite clasts (**Fig.12f**).
577 Cathodoluminescence imaging reveals that the clasts in the foliated cataclasites have a similar purple CL
578 color as the large white jadeitite clasts, confirming their genetic link (**Fig.12a,b,c**). These clasts are
579 rimmed by two distinct clinopyroxene compositions (Jd_2 and *Omp*) with increasing omphacitic content
580 (**Fig.11e, 12f**), the interfaces between

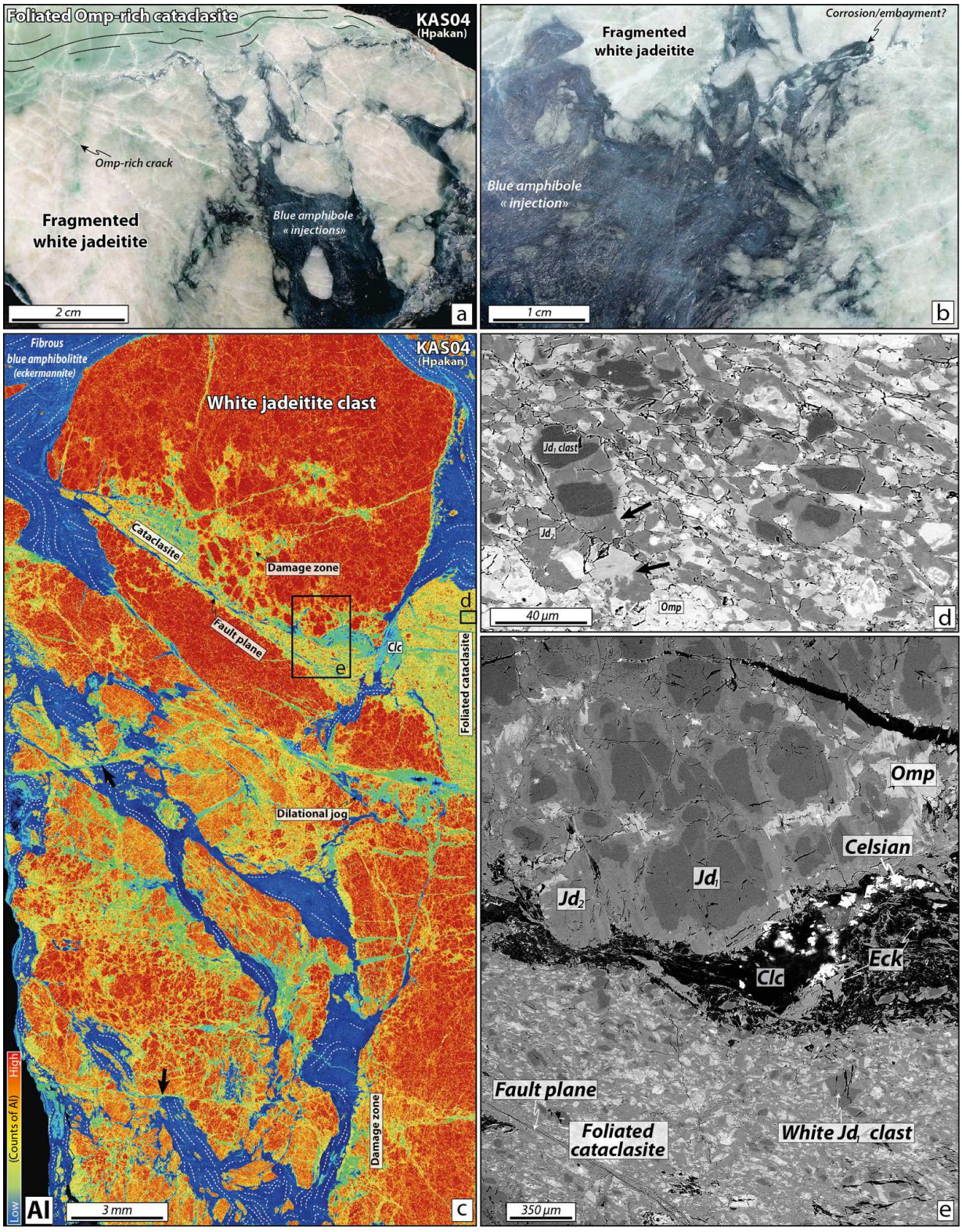
Foliated Omp-rich cataclasite
KAS04
(Hpakan)
Omp-rich crack
Fragmented
white jadeitite
Blue amphibole
« injections»
2 cm
a
Fragmented
white jadeitite
Corrosion/embayment?
Blue amphibole
« injection»
1 cm
b
Fibrous
blue amphibolitite
(eckermannite)
KAS04
(Hpakan)
White jadeitite clast
Cataclasite
Damage zone
Fault plane
d
e
Clc
Foliated cataclasite
Dilational jog
Damage zone
Low
(Counts of Al)
High
Al
3 mm
c
Jd1 clast
Jd2
Omp
40 µm
d
Omp
Celsian
Jd1
Jd2
Eck
Clc
Fault plane
Foliated
cataclasite
White Jd1 clast
350 µm
e

581

Figure 11. a. Polished hand specimen of a brecciated jadeitite from Myanmar (KAS04), where white jadeitite clasts are transected by a green, strongly foliated cataclastic domain (Type II). The sample is lately affected by a stage of pervasive, fibrous sodic amphibole (eckermannite) growth, infiltrating along cracks. b. Higher magnification image showing how the white jadeitite has been hydrofractured and filled by sodic amphibole, leaving embayments that may be interpreted as resulting from the dissolution by a reactive fluid. Note also the distribution of sodic amphibole fibers infiltrating the Type III breccia. c. EDS X-ray map (counts of Al) showing the great complexity of the internal structure in sample KAS04, where several brittle deformation and fluid-rock interaction events can be identified, including deformation features along ancient fault planes with injecting cataclastic material as well as damage zone formation. d. BSE image of the foliated cataclasite domain where white Jd_1 clasts are now dissolved and embedded within a Jd_2-omphacite matrix. e. BSE close-up image of the faulted area in panel c showing the foliated cataclasite domain, the micro-fault plane as well as the partly re-equilibrated damage zone. The contact between the large white jadeitite clast has been re-activated and filled by a clinochlore-eckermannite-celsian paragenesis.

which appear to be dissolved (see black arrows on **Fig.11d**).

Elongated patches with omphacitic composition are aligned with the main foliation, and invade the fault as well as its damage zone (**Fig.12a,b**). The foliated nature of this fine-grained jadeite-omphacite rich domain is evidenced using EBSD mapping (**Fig.12d**). This image shows a shape-preferred orientation, with elongated jadeitic clinopyroxene grains (aspect ratios up to 6:1) defining a lineation subparallel to the strong crystallographic-preferred orientation well visible in [001] (**Fig.12e**). Similarly to Polar Urals jadeitites, the [010] crystallographic axes are highly concentrated normal to the foliation plane but [100] are aligned within the foliation plane perpendicular to [010]. This defines a fabric akin to LS-type tectonites, confirming the likely presence of crystal-plastic deformation mechanisms associated with a near-plain strain geometry, as also supported by experimental investigations and numerical simulations (Ulrich & Mainprice, 2005; Zhang et al., 2006). In addition, intragranular misorientation maps show that several highly misoriented grains are surrounded by clusters of finer-grained crystals devoid of internal

608 deformation. The former likely represent remnant fragments, and the latter dynamically recrystallized
609 grains along the foliation (**Fig.12d**, **Fig. S3**).

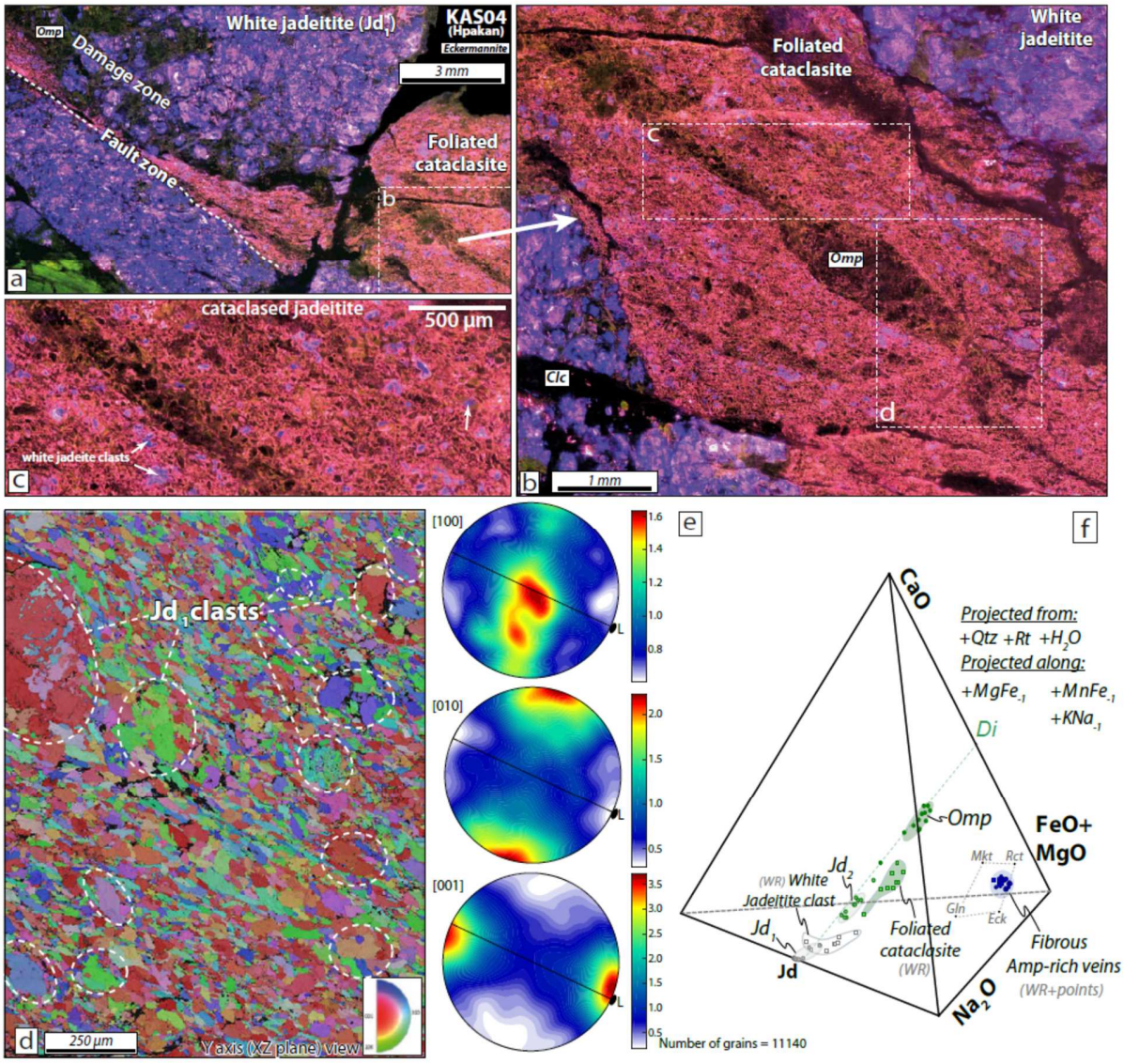

610

611 **Figure 12. a, b, c.** Cathodoluminescence images showing the relationships between the different textural
612 domains of sample KAS04. Note how the *Jd*$_1$ fragments (pink colors) are dragged within the foliated
613 cataclasite domain. **d**. EBSD orientation map colored according to the inverse pole figure key (IPF) of
614 jadeite (bottom right), showing a shape preferred orientation of jadeite to the X direction of the strain
615 ellipsoid (i.e., stretching orientation). View (XZ plane) corresponding to the Y axis of the finite strain
616 ellipsoid. **e**. Pole diagrams of jadeite crystals smaller than 100 µm in diameter (larger crystals are
617 considered as clasts, as indicated in the figure and more detailed in **Fig. S3**), represented in an upper

hemisphere equal-area projection for [100], [010] and [001] crystallographic axes. Contours are multiples of uniform density distributions. The bold dot on the L axis represents the stretching lineation direction (X direction of the strain ellipsoid) and the black line the foliation plane. **f**. Projection in a CaO-Al_2O_3-(FeO+MgO)-Na_2O system of the different groups of mineral compositions, as well as local surface estimates of bulk major element composition (WR: whole-rock). Circles are single point measurements and squares are SEM-based surface compositional estimates (WR).

A late faulting event that led to the precipitation of blue amphibole as well as clinochlore along micro-fault planes affects the white jadeitite domain and the foliated cataclasites (**Fig.11c,e**). Celsian crystals (a Ba-rich feldspar) are commonly found texturally associated with these apparently late clinochlore-bearing fault zones (black arrows on **Fig.11c**). To summarize, textural relationships visible in sample KAS04 suggest the following deformation sequence: (i) tectonic brecciation of the white jadeitite; (ii) cataclasis of some of the white jadeitite and foliation of this cataclased domain; (iii) re-brecciation (hydraulic) of the volume and precipitation of the Na-amphibole-rich domain between brecciated and cataclased domains; and (iv) crystallization of clinochlore and celsian along late discrete fault zones oblique to the previous fault structures (**Fig.11c**).

9. Discussion

9.1 Worldwide jadeitites record mixed deformation regimes

Our comparative and analytical investigation reveals that most of the studied samples from Russia, Guatemala and Myanmar display widespread and similar markers of fracturing that have received little attention in previous studies (e.g., Dobretsov & Ponomareva, 1968; Shi et al., 2009b). Brittle deformation markers span a broad range, from Type I breccias typical of damage zones (e.g., **Figs.2, 6, 10a, 13a**), to Type II variably foliated cataclasites that are more diagnostic of strongly localized fault systems (e.g., Rowe et al., 2011; Angiboust et al., 2015; Oncken et al., in revision; **Figs.5, 9, 13b**), to Type III hydraulic breccias thought to develop at high fluid pressure conditions as extensional veining (e.g. Woodcock et al., 2007). A common feature of all studied materials are arrays of healed mineral fractures commonly

coupled with grain size reduction, crystal indentation and dissolution-precipitation processes. This pattern, sometimes hardly visible using optical microscopy, requires the use of specific analytical approaches such as cathodoluminescence imaging or electronic microscopy to be documented (e.g., **Figs.3, 12**; Shi et al., 2003; Sorensen et al., 2006; Takahashi et al., 2017). Pure extensional fracturing (e.g., hydrofracturing; Type III; **Fig.13c**) has been identified in several samples, with fragments of the host that appear to have been snatched into clinopyroxene or amphibole-rich veins (**Fig.10b**). When several brittle events can be distinguished, Type III events always occur late in the sequence (**Table 1**). In all localities, it is always the original white jadeitite material (Jd_1) that undergoes shearing-related brecciation and subsequent cementation by a darker clinopyroxene (Jd_2 or *Omp;* **Fig.7e**) and/or by sodic amphiboles (e.g., eckermannite; **Figs.7f, 11a**).

Evidence for viscous deformation has been observed in a shear band transecting the coarse-grained Polar Urals white jadeitite body (**Fig.4a**), as well as within Myanmar jadeitites (Shi et al., 2009b). This observation reveals that the white jadeitite body, once crystalized, underwent differential stresses high enough to generate crystal plasticity (most likely via dislocation creep) yielding a CPO. Following the argument developed in Angiboust et al. (2021), it is hypothesized that this shearing occurred at c. 650 °C, i.e., above the antigorite stability field (**Fig.14d**), because no evidence for Cr enrichment was found in this shear band (even though other processes may also contribute to Cr availability in the system; e.g., Huang et al., 2019). Assuming a strain rate of 10^{-14} s^{-1} (a median value commonly inferred for ductile shear zones; e.g., Pfiffner & Ramsay, 1982) and using the experimentally-based dislocation creep flow laws from Orzol et al. (2006) and Zhang et al. (2006), it is possible to estimate the differential stresses required for creating the shear band of sample UR03 to be between 125 and 40 MPa, respectively. Note that these values likely represent an upper bound since other competing deformation mechanisms such as pressure solution creep would likely be activated at lower stress values (e.g. Godard & Van Roermund, 1995). The implications of these values will be discussed hereafter.

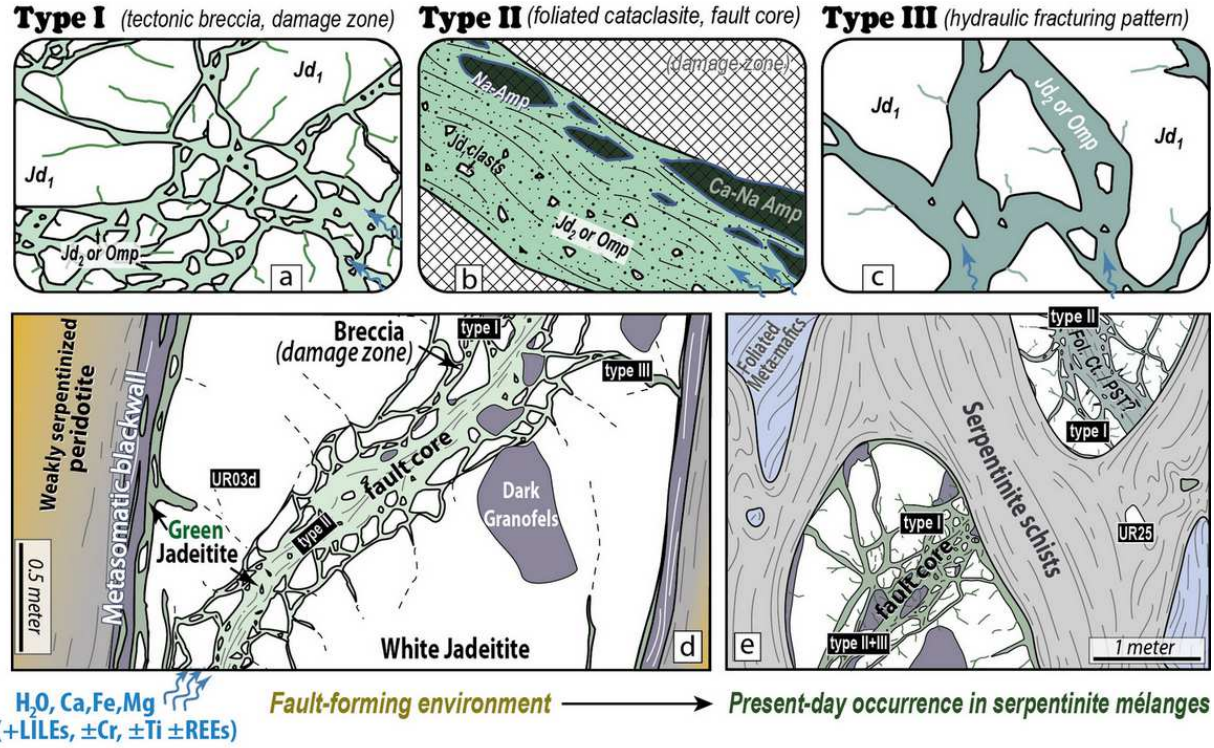

667

668 **Figure 13. a, b** and **c.** Sketches showing the key features of the three main categories of tectonized
669 jadeitites identified in this comparative study. **d**. Sketch depicting the white jadeitite structure (derived
670 from observations from the Pus'yerka body) at the time of brecciation, indicating the various elements
671 identified in the field and their position with respect to the main fault and host ultramafics. **e**. Sketch
672 highlighting the structure of jadeitite blocks as exposed in HP-LT serpentinite mélanges, where they are
673 commonly associated with blueschist and/or eclogite-facies crustal rocks. We posit that the faulting
674 frequently observed within jadeitite blocks has been acquired earlier, when the jadeitite was a dyke-like
675 structure hosted by weakly serpentinized mantle wedge peridotites.

676

677 The CPO observed in KAS04 sample and other Type II samples likely results from a combination
678 of dislocation creep and solution-precipitation processes in a dominant simple shear regime but also
679 with some degree of pure shear, as suggested by the observed LS-type fabric but also a weak girdle of
680 [001], respectively (**Figs.4c,12e**). These deformation mechanisms have been already documented in
681 eclogite-facies clinopyroxene by Godard & Van Roermund (1995; see also Ulrich and Mainprice, 2005)
682 (e.g., **Fig.12b**). It is clear from the fragmented jadeitite clast distribution (along with the

683 cathodoluminescence color of the various crystals; **Fig.12b**) that cataclastic flow (during brittle
684 deformation) operated through localized faulting *before* CPO formation (see also Oncken et al., in
685 revision; **Fig.10c**). In other words, we infer that the observed foliated cataclasite structure is the
686 protracted result of consecutive brittle flow followed by slower, viscous creep. This sequence of events
687 may be the record of one or several seismic cycles where fast co-seismic slip is immediately followed by
688 a slower after-slip event (e.g., Sibson, 1986; Rowe et al., 2011). Indeed, many of the reported fabrics
689 resemble the structures documented in fault cores at shallower/colder environments where multiple
690 episodes of particle fluidization are reported on the principal slip zone (**Figs.5f, 10c**; e.g., Sibson, 1986;
691 Snoke et al., 2014; Cox & Munroe, 2016; Muñoz-Montecinos et al., 2021a). Interestingly, the main
692 brecciation/cataclasis event in sample KAS04 is followed by an episode of hydraulic brecciation where
693 Na-amphibole precipitates Type III; **Fig. S2**). Similar deformation patterns have been observed in dark
694 granofels that also comprise breccias (**Fig.6**), foliated cataclasites (**Fig.5**) and multiple fracturing events
695 (**Fig.3c**; **Fig. S5; Table 1**).

696 Exceptionally, the finding of elongated spherulitic shards in a fine-grained sheared domain
697 (**Figs.7c,9d**) – possibly formed by the devitrification of former glass fragments – may be indicative of
698 former pseudotachylytes (i.e., a glassy injection domain formed by melting during fault slip at seismic
699 strain rates; e.g., Austrheim & Boundy, 1994; Austrheim & Andersen, 2004). The *Jd1* clasts found floating
700 in the comminuted matrix display extensive fracturing, grain-size reduction and stress-driven corrosion
701 that characterize pseudotachylyte-bearing systems (e.g., Kirkpatrick & Rowe, 2013). Glassy shards similar
702 to those shown in **Fig.9g** are mostly reported in ignimbrite deposits (e.g., Bull & McPhie, 2007) and in
703 rocks from ancient impact craters (e.g., Dressler & Reimold, 2001). Although, to the best of our
704 knowledge, such shard-like textures have not been described in ancient fault zones, the discovery of
705 unreported textures must be expected because the formation environment of these slip events strongly
706 differs from other paleo-earthquake reports made in the downgoing lithosphere (see below).

9.2 Jadeitite formation and pressure-temperature conditions of brittle deformation

In most serpentinite mélange settings, the original structure at the time of jadeitite formation has been obliterated or disrupted by subduction zone tectonics (e.g., Harlow et al., 2015). Whereas in several cases jadeitites appear to be directly precipitated from hydrothermal fluids ("P-type" jadeitite, according the classification from Tsujimori & Harlow, 2012; e.g., Garcia-Casco et al., 2009; Harlow et al., 2011), some localities preserve textural features typical of a replacement process ("R-type" jadeitite according to the same classification), including igneous zircon crystals with older crystallization ages (Yui et al., 2012; Hertwig et al., 2016) or the presence of incompletely "jadeitized" trondhjemitic remnants in the dyke volume (Angiboust et al., 2021). Indeed, early observations from Dobretsov & Ponomareva (1968) and Kuznetsov et al. (1986) in Russia, as well as Bleek (1908) and Chhibber (1934) in Myanmar, reveal that original jadeitite may form as dyke-like structures. It is plausible that these dykes were jadeitized during long-term cooling within the high-pressure field, coeval with replacement of a former felsic intrusive body formed earlier in the mantle wedge above the subduction interface, and possibly shortly after subduction initiation in a warm thermal regime (see the recent model by Angiboust et al., 2021; see also Meng et al., 2011 and **Fig.14**). Such secular cooling has also been documented above the metamorphic soles from New Caledonia (e.g. Soret et al., 2016) and Oman ophiolites (e.g. Prigent et al., 2018).

A number of recent studies (e.g., Garcia-Casco et al., 2009; Schertl et al., 2012; Angiboust et al., 2021) have suggested that jadeitites may commonly form at temperatures far above 500 °C, perhaps up to 700 °C. Garcia-Casco et al. (2009) and Cárdenas-Párraga et al. (2012) have also suggested that exsolution features, as observed in sample KAS10 (**Fig. S2**), could evidence the cooling of a clinopyroxene of intermediate jadeite-omphacite composition below the solvus at 500 °C. This implies that white jadeitites including the Myanmar samples formed at temperatures higher than generally expected. Consistent with this interpretation, Harlow & Sorensen (2005) suggested that the whitish color of the

731 relatively high temperature jadeitite may be due to Cr stability in the host ultramafic chromite and
732 clinopyroxene crystals. In other words, it is likely that Cr-poor white jadeitite bodies formed at T
733 conditions above the antigorite stability field, i.e., before serpentinization of the host ultramafic (**Fig.14**),
734 even though some Cr may also be hosted in high temperature chloritite blackwall (not documented in
735 the studied localities; see Cardenas-Parraga et al., 2012). Following this logic, it can be concluded that
736 the systematic observation of darker-shaded clinopyroxene precipitates/overgrowths within breccias or
737 cataclasites in many jadeitite localities indicate that fracturing and fluid-rock interaction events occurred
738 during long-term cooling at T<600 °C (e.g., Garcia-Casco et al., 2009; Schertl et al., 2012; this study).

739 Whereas breccias and cataclasites are classically reported for rather shallow – and hence colder –
740 environments (<15 km depth, T<300 °C; Sibson, 1986), a number of field examples have recently shown
741 that such features can form at depths greater than 30 km in the downgoing subducted crust (e.g.,
742 Angiboust et al., 2012; 2015; Hertgen et al., 2017; Muñoz-Montecinos et al., 2021a; Oncken et al., in
743 revision). Minerals filling the studied breccias and growing within these fault zones encompass (i)
744 omphacite (and locally lawsonite) in Guatemalan samples; (ii) omphacite, jadeite, phlogopite and Na-rich
745 amphiboles in the Polar Urals samples; and (iii) Na-amphiboles, jadeitic and omphacitic clinopyroxenes in
746 Myanmar samples. These parageneses point to HP-LT conditions ranging between 1–2 GPa and 300–500
747 °C as documented in the reviews of Tsujimori & Harlow (2012) and Harlow et al. (2015; **Fig.14d**).
748 Angiboust et al. (2021) have demonstrated that the phlogopite-bearing fracturing event seen
749 crosscutting Polar Urals jadeitites occurred at least 15 Ma after the HT jadeite-forming event (see also
750 Meng et al., 2011), thus providing an independent confirmation of the secondary nature of the
751 brecciation process. We conclude that in the studied set of samples – and perhaps as a rule in fossil and
752 active subduction systems – brittle deformation of jadeitites is a deep process occurring at or near peak-
753 burial depths in a cooling environment (as suggested in **Fig.14**), rather than as a consequence of late
754 exhumation-related deformation. In order to undergo brittle deformation, the rock must be in-situ and

surrounded by mechanically strong material, rather than as a tectonic block floating in a serpentinite-matrix mélange where stress is dissipated in the weak matrix.

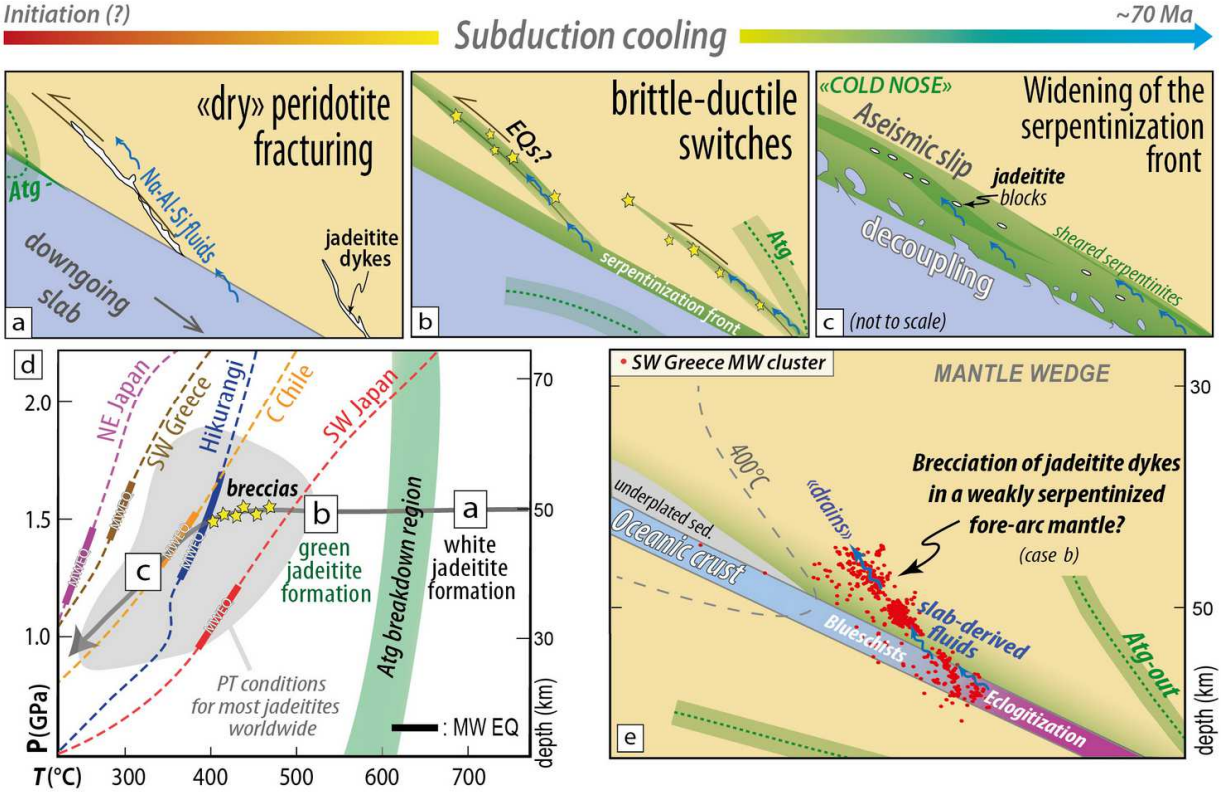

Figure 14. a, b and **c.** Sketches depicting the long-term tectonic evolution of jadeitite "dykes" along the base of the mantle wedge, from their formation (by replacement of a previous dyke structure or from direct precipitation from a fluid) to their fracturing, dismembering and wrapping as blocks in a chaotic serpentinite mélange. Previous geochronological data (Angiboust et al., 2021) confirms that several tens of millions of years of subduction activity and mantle wedge hydration are required to achieve a structure as shown in panel (c). Atg-: antigorite dehydration reaction. **d**. Pressure-Temperature diagram indicating the conditions of formation of the main white jadeitite bodies documented worldwide, and the conditions of the green jadeitite tectonic overprint (and associated sodic amphibole generation). After, and only after brecciation (yellow stars), the dyke fragments can be exhumed along the plate interface, provided that the hangingwall serpentinization rate is sufficiently high to enable return-flow of these dense blocks in a buoyant, serpentinized matrix (e.g., Gerya et al., 2002; Guillot et al., 2009). P-T conditions for jadeitites

770 are sourced from the compilations by Tsujimori & Harlow (2012) and Harlow et al. (2015). Also shown are
771 the slab-top temperature estimates as calculated by Antriasian et al. (2019, Hikurangi), Wang et al. (2020,
772 central Chile), Halpaap et al. (2019, W Greece) and Peacock (2003, NE and SW Japan). References used for
773 the depth of mantle wedge earthquakes (MW EQ) are provided in text. **e**. Location of one of the MW
774 clusters identified by Halpaap et al. (2019) in W. Greece and interpreted as marking the trace of plate-
775 interface fluids migrating along a vent structure. The formation of this EQ nest (corresponding to the
776 yellow stars from panel d) likely implies that the serpentinization ratio of the subduction interface hanging
777 wall is very low, thus pointing to a structure analogous to the sketch drawn in panel (b).

778 *9.3 Origin of brecciated dark granofels and relationships with fluid-rock interaction events*

779 A striking similarity characterizes the textural relationships between the dark granofels and
780 jadeitites from the Polar Urals and Myanmar. In both localities, they occur as thin layers or pods of
781 "amphibolites" of several tens of centimeters (Chhibber, 1934; Angiboust et al., 2021; **Fig.1e**), generally
782 striking parallel to the main "dyke" foliation and deformed coeval with the associated jadeitites. Their
783 amphibole compositional patterns are also nearly identical, with relicts of Ca-rich amphiboles in the
784 granofels mineral cores (mostly edenite and Mg-katophorite), and Ca-poor, Na-rich amphiboles along
785 their rims and along highly metasomatized domains (Shi et al., 2003; **Fig. S2**). Field observations
786 (Chhibber, 1934; Angiboust et al., 2021) and petrological investigations suggest that two distinct dark
787 granofels occurrences may exist: (i) as disaggregated fragments (the "schistose amphibolite inclusions"
788 from Chhibber, 1934; see also Harlow et al., 2015) inherited from a pre-jadeitization event; and (ii) as
789 amphibole-rich blackwalls formed at the contact between the jadeitite body and the host ultramafic (Shi
790 et al., 2003). The latter should in theory have formed lately at T<350 °C (Shi et al., 2003) and only exhibit
791 Na-amphiboles (since no Ca chemical potential gradient exists between ultramafics and jadeitites), thus
792 hampering the formation of calcic and sodic-calcic amphiboles such as edenite or Mg-katophorite in the
793 reaction blackwall. The former should instead contain these sodic-calcic amphibole species (e.g.,
794 **Figs.5a,6b,10a**) as remnants of an early HT event, associated with the infiltration of alkali-rich fluids
795 and/or melts (likely trondhjemitic in composition) within ultramafics in a subduction initiation setting.

This process is known to occur in anomalously high subduction thermal regimes (see also the discussion in Angiboust et al., 2021 and similar structures and rock assemblages in Lazaro et al., 2011 and Soret et al., 2016). Brecciation, followed by boudinage, late tectonic disaggregation and block-in-matrix deformation, most likely blurred the primary contacts, hampering an accurate reconstruction of the geometry of the original jadeitite-dark granofels boundaries (e.g., **Fig.10a**).

9.4 Fluid ingress and metasomatic imprint

A common feature reported in jadeitites worldwide is the enrichment in Ca, Fe and Mg of jadeitic clinopyroxenes due to the infiltration of Ca-Fe-Mg-rich fluids associated with dissolution-precipitation processes during late fluid-rock interaction events (e.g., Sorensen et al., 2006; Garcia-Casco et al., 2009; Harlow et al., 2011; Cardenas-Parraga et al., 2012; Angiboust et al., 2021; this study). The formation of dissolution features (**Fig.3c**), re-equilibration of clast rims (**Fig.8a**) and the metasomatic overprint left in the rock record (**Fig.9b**) are witnesses to the apparently corrosive nature of the infiltrating fluids, which were at thermodynamic disequilibrium with respect to the infiltrated material. The absence of carbonates in most jadeitite occurrences suggests that the fluids were CO_2-poor, most likely because the CO_2 precipitated as carbonates before reaching the jadeitite-forming location. Substantial Cr enrichments are also visible in some of the sheared domains and between breccia fragments (as shown for instance by the growth of chromian spinel around Mg-katophorite clasts in sample UR11b; **Fig.6b**; see also the green overgrowths around white jadeitite clast in **Fig.7f**).

As discussed earlier, the release of Cr may be related to serpentinization of the host peridotite during fluid-rock interaction. It is important to note that (i) jadeite/omphacite is found growing within brecciated white jadeitites (**Figs.3b, 8a and 11c**) and amphibole-rich dark granofels (**Fig.6d**); and (ii) amphibole growth is observed in brecciated dark granofels (**Fig.5b**) and between white jadeitite breccia fragments (**Figs.7f,11a,11b**). From these observations, it appears that the incoming fluid composition

819 was not buffered by the wall-rock composition and that brittle events contributed to a chemical and
820 mechanical homogenization of the original dyke-forming lithologies. Furthermore, the widespread
821 formation of texturally late micas (e.g., phlogopite in the Polar Urals: Angiboust et al., 2021, see also **Fig.**
822 **S1**; phengite or phlogopite in Guatemala: Harlow et al., 2011; Flores et al., 2013; white mica in W. Japan:
823 Shigeno et al., 2012) associated with enrichments in LILEs and other fluid mobile elements (**Figs. S3 and**
824 **S4**) confirm that fluid sources were variable in time, switching from a mafic oceanic crust signature to a
825 more hybridized composition with transient highs in sedimentary input (e.g., Sorensen et al., 2006, 2010;
826 Morishita et al., 2007; Meng et al., 2011, 2016; Harlow et al., 2015; Chen et al., 2018; Cardenas-Parraga
827 et al., 2012). This temporal variability of incoming fluid chemistry from a more mafic to a more
828 sedimentary signature could likely be explained by variations in the amount of sedimentary material
829 undergoing devolatilization reactions in the underlying subduction channel (e.g., Bebout, 2007;
830 Scambelluri et al., 2019). This chronological sequence confirms that the same fluid pathways (namely the
831 jadeitite "dykes") were used over several millions of years as major drains for highly pressurized plate-
832 interface fluids, on their way to the partly hydrated mantle wedge (e.g. Doglioni et al., 2009; Spandler &
833 Pirard, 2013).

834 The distribution of jadeitite "dykes" as seen in the Polar Urals (**Fig.1b**; see also Angiboust et al.,
835 2021) demonstrates that fluid pathways are rather discrete in the overlying plate (i.e., jadeitite does not
836 precipitate randomly everywhere in the fore-arc mantle). It also indicates that less mechanical energy is
837 required to re-fracture a pre-existing physical discontinuity (e.g., a dyke-like structure) than creating new
838 channels for draining plate-interface fluids. This implicitly requires that breccia sealing must have been
839 faster than rupture recurrence to explain the mutual crosscutting relationships documented between
840 the various events identified in our study (see also Woodcock et al., 2007). It seems clear that nearly
841 lithostatic pore fluid pressure was sustained throughout the entire jadeitite drain activity as
842 demonstrated by the ubiquitous evidence for fluid-rock interaction in the three types of brittle features

reported here (**Table 1**; see also Kuznetsov et al., 1986 and Angiboust et al., 2021). Yet, transient overpressures likely triggered the formation of some of the (explosive) breccia features (Type III) within already-tectonized Type I and Type II domains (**Figs.11c,13a,b**). These findings are consistent with the episodic opening of vein systems and filling of voids by omphacitic compositions documented by Garcia-Casco et al. (2009) and Cardenas-Parraga et al. (2012) in the Sierra del Convento serpentinite mélange (E. Cuba), and also in other subduction HP-LT mélanges environments (e.g., Muñoz-Montecinos et al., 2021b).

9.5 Insights on slip properties in a fluid-saturated mantle fault zone

Brecciated rocks have long been recognized as potential markers of seismic deformation (e.g., Sibson, 1986; Angiboust et al., 2012; Melosh et al., 2014). Evidence of fault-zone rocks with diagnostic elements such as damage zones and fault cores (**Fig.13a, b**) highlights for the first time that jadeitites (and associated dark amphibole-rich granofels) host abundant brittle deformation events, most likely along fast-slipping seismogenic fault planes. Estimating slip or strain rates along paleo-fault surfaces (or shear zones) is a challenging task, subject to great uncertainties. While Oncken et al. (in revision) have recently demonstrated that foliated cataclasites can form in slow slip environments for strain rates in the range 10^{-3} to 10^{-5} s^{-1}, the lack of well-preserved pseudotachylytes in the studied samples hampers a direct identification of seismic slip rates (i.e., on the order of m/s). However, the discovery of a foliated fault zone with abundant "shards" exhibiting structures analogous to devitrified spherulites (**Fig.9g**) opens the possibility for constraining former slip events at strain rates approaching seismic slip velocities, fast enough to generate co-seismic temperatures as high as 1500 °C (e.g., Sibson et al., 2006; Menant et al., 2018) and trigger frictional melting. Note that chemical modification of the system is required to explain the enrichment in Ca, Fe and Mg of the shard-bearing fault zone as shown in **Fig.9b, c.** As earlier stated by Magloughlin (1992) and Swanson (1992), cataclasites and pseudotachylytes may be closely intricated in fault zone rocks, both exhibiting evidence for open-system modification of the

867 pristine host composition. Thus, the structures herein observed may have formed through (i)
868 metasomatic fault-zone alteration associated with fluid influx within a finely-crushed cataclastic domain
869 (likely a structure as shown in **Fig.13b**), followed by (ii) fast-slip along narrow zones where local melting
870 of the previously-formed cataclasites occurred (thus explaining the enrichment in omphacitic component
871 of "shards" and devitrified spherulites, **Fig.9d-h**). Subsequent shear deformation contributed to the
872 apparent banding systematically observed in Type II fault rocks (e.g., **Fig.9b**). It is therefore proposed
873 that the reported features can be explained by fluctuations in slip rate velocities in a fluid-saturated fault
874 zone.

875 *9.6 Implications for mantle wedge seismicity and plate-interface rheology*

876 Observations made on the Myanmar and Guatemalan loose samples are challenging to link to
877 their respective formation context because pristine field relationships were obliterated during block-in-
878 matrix dismembering as well as sedimentary transport into conglomerate deposits. A few exceptional
879 observations in Myanmar document the presence of jadeitite-bearing "dykes" that are several hundred
880 meters long and meters to tens of meters thick (e.g., Bleek, 1908), but most of these bodies have been
881 mined. The Polar Urals Pus'yerka locality (and to a lesser extent other jadeitite localities in Siberia;
882 Dobretsov & Ponomareva, 1968) has the potential to yield in situ information on the dimensions of
883 ruptured bodies as well as refining the chronology of the processes at stake. Kuznetsov et al. (1986)
884 report that jadeitite "dykes" in the Pus'yerka locality (also mined in the 1990s and mostly exhausted)
885 were locally up to several tens of meters thick, pinching out to meter-thick bands at the northern and
886 southern terminations of the several kilometer-long dyke structure (**Fig.1b**). These observations provide
887 critical insights into the minimum size for mantle wedge earthquakes. Assuming a planar geometry for a
888 single event that ruptured the Pus'yerka jadeitite body (before the dyke structure was boudinaged), a
889 squared 3x3 km rupture, a 10 cm co-seismic displacement and a shear modulus of 84 GPa for jadeitite
890 (Hao et al., 2020), a magnitude of $M_w = 4.5$ can be calculated (Sibson, 1989). This magnitude estimates

891 ranges between 3 and 5 when changing fault dimensions and displacements within bounds compatible
892 with field and structural observations.

893 Is this range of magnitudes comparable with the events reported in the forearc lithospheric
894 mantle clusters in active subduction zones? Davey & Ristau (2011) report a subvertical, 10 km-large
895 cluster of earthquakes (average maximum magnitude of 4.5 for normal, inverse and strike-slip events)
896 above the subduction interface at 40–50 km depth in the northern Hikurangi margin. These authors note
897 their spatial relationship with the inferred 700 °C isotherm, where they expect full antigorite breakdown
898 and relate these earthquakes to dehydration embrittlement processes. Released upwelling fluids
899 infiltrate the mantle wedge, possibly explaining volcanism in the above back-arc basin. Nakajima &
900 Uchida (2018) have identified a nest of supra-slab micro-seismicity (M_w= 1–3) located 10-15 km above
901 the Philippine plate in central Japan, between 25–35 km depth with focal mechanisms corresponding to
902 normal and strike-slip events. Interestingly, seismic activity markedly increased after the 2011 Tohoku
903 megathrust rupture, leading Nakajima & Uchida (2018) to consider these events as marking the trace of
904 highly pressurized fluids, cyclically drained above the plate interface along a "highly fractured, pre-
905 existing mature pathway". According to this model, several months are required for these fluid pulses to
906 travel the few kilometers that separate these nests from the megathrust area (see also White et al.,
907 2016). Similar structural conclusions were drawn by Yu and Zhao (2020) who focused on 35–55 km depth
908 microseismicity events in the NE Japan forearc mantle using P-wave velocity perturbations. Halpaap et
909 al. (2019) have demonstrated that several seismicity nests ranging in magnitude from 2–4 occur under
910 Western Greece in a weakly serpentinized mantle. These events (mostly extensional) occur between 45–
911 55 km depth along a diffuse structure that dips at 45° to the subduction interface plane (see hypocenter
912 distribution plotted in **Fig.14e**). Halpaap et al. (2019) conclude that plate-interface fluids transiently
913 migrate along fault-bounded vents, diminishing the pore pressure along the interface, thus decreasing
914 plate-interface seismicity. This non-exhaustive list of studies confirms that fluids are unequivocally

915 required to explain the seismotectonic features documented in the remote mantle wedge. It also
916 appears that these nests are transient in the context of subduction zone evolution and spatially localized
917 within well-defined structures.

918 The formation of mantle wedge earthquakes has critical implications for plate-interface rheology and
919 more specifically may provide precious constraints on the volumetric abundance of serpentinite in the
920 forearc mantle. A vibrant debate exists on the abundance and distribution of serpentinite in the mantle
921 wedge based on the interpretation of seismic wave velocity perturbations and the effect of serpentinite
922 anisotropy (e.g., Hyndman & Peacock, 2003; Liu et al., 2020; Luo & Wang, 2021). It is likely that
923 serpentinite distribution is highly uneven in the mantle wedge, with the highest serpentinization rates
924 directly above the interface and fairly low rates (likely less than 15 vol.%) within the innermost forearc
925 mantle (e.g., Reynard, 2013; Abers et al., 2017; Halpaap et al., 2019). Stress accumulation in the mantle
926 must be inhibited by serpentinite formation, which is known to flow at very low stresses (e.g., Escartin et
927 al., 2001; Reynard, 2013 and references therein). The stress level required for enabling plastic
928 deformation of jadeitites (40–125 MPa according to our calculations) is several orders of magnitude
929 greater than the stresses required for the flow of serpentinites (approximately 1 MPa at 600 °C using the
930 calibration from Hilairet et al., 2007). In order to transfer plate-interface stresses into the overlying
931 mantle and trigger plastic deformation of jadeitites (**Fig.4**), the host peridotite must have been relatively
932 dry (i.e., with serpentinization rates far lower than 10 vol.%.) as inferred for many active subduction
933 settings (e.g., Abers et al., 2017; Halpaap et al., 2019). The triggering of multiple cataclastic events as
934 documented by our observations (**Fig.9b**) could be explained by transient increases in strain rate (during
935 slow slip events or earthquakes), by an increase of pore fluid pressures, or by a combination of both. The
936 latter option is supported by the discovery of fabrics typically observed in faulted jadeitites (e.g., **Figs.9,**
937 **12**), as well as major and trace element chemical arguments that point to mass transfer and opening of
938 the system to external fluids (e.g., **Fig.6**), most likely sourced in the subduction interface region.

From these considerations, we can conclude that (i) the seismic events recorded above the subduction interface in several active subduction zones likely correspond to the brittle deformation of jadeitite bodies (**Fig.14d,e**), which according to field observations are themselves derived from the metasomatic replacement of former felsic dyke bodies or direct precipitation from fluids (see discussion in Harlow et al., 2015 and Angiboust et al., 2021); and (ii) brittle jadeitite deformation may have occurred in the fossil subduction record and in present-day settings in a relatively dry peridotitic mantle, thus providing valuable insights into the serpentinization degree of the interface hangingwall and the stress distribution at the base of the megathrust region (Halpaap et al., 2019; Luo & Wang, 2021). This record of the deep conduits draining plate-interface fluids into the overlying mantle wedge sheds light on the structure of the "cold nose" above the subduction interface, with implications for volatile budget estimates, the rheology of the plate interface itself (including the various types of seismicity), and the interpretation of Vp/Vs and Poisson's ratios from active subduction settings worldwide.

10. Conclusions

A vein network from the Polar Urals composed of jadeitite and amphibole-phlogopite granofels is hosted in mildly serpentinized peridotites. This structure formed by metasomatic replacement of a former magmatic dyke above the subduction interface at c. 50 km depth, in a young and dry mantle wedge environment. During subsequent cooling of the subduction zone, this jadeitized "dyke" experienced mixed brittle-viscous deformation regimes associated with several serpentinite- and oceanic crust-derived fluids. Extensive fracturing, well-visible in the amphibole-rich granofels and more cryptic in the jadeitite bodies, led to the local formation of breccias and foliated cataclasites. The associated metasomatic imprint confirms the importance of these fault zones as major drains for overpressurized plate-interface metamorphic fluids. Very similar features, including omphacite- and amphibole-rich breccias together with foliated cataclasites, are also observed in loose jadeitite boulders from Myanmar and Guatemala serpentinite mélanges. We propose that supra-slab seismicity nests recorded in present-day subduction margins (e.g., N Hikurangi, NE Japan, W Greece) may reflect the repeated fluid-assisted breakage of planar bodies formed by jadeitite "dykes". The local presence of these rupture events implies that the serpentinization rate was locally low (probably <10–15 vol.%) along the base of the

mantle wedge during “dyke” faulting activity. These results shed light on the importance of physical discontinuities such as jadeitite bodies for draining plate-interface fluids into the mantle wedge, and provide key constraints on the stress distribution in deep subduction margins.

Acknowledgements

Johannes Glodny (GFZ Potsdam) is acknowledged for insightful discussions that initiated this project. François Gendron (MNHN) is also warmly acknowledged for sharing his knowledge about the Motagua region and information on archeological material. Ksenia Kulikova is thanked for sharing her knowledge on the regional geology of the Urals. J.M-M express his gratitude to Ralf Hielscher, Rüdiger Kilian and Luiz Morales for assistance with the MTEX software. Michael Popov, Stephan Borensztajn, Arthur Delorme, Julia Cozzolino and the Camparis team are acknowledged for technical assistance. Michael Bostock and Gaston Godard are acknowledged for insightful discussions. The careful and efficient editorial handling by Carlo Doglioni is much appreciated. Comments from Bill Leeman and two anonymous reviewers helped to greatly increase the clarity of this manuscript. D.D. was funded by the European Research Council grant REALISM (2016-grant 681346) to Alexandre Schubnel. This study was funded with an IDEX-USPC research chair grant (#16C538) and was partly supported by the IdEx Université de Paris ANR-18-IDEX-0001. This is IPGP contribution #40xx.

References

Abers, G. A., Van Keken, P. E., & Hacker, B. R. (2017). The cold and relatively dry nature of mantle forearcs in subduction zones. *Nature Geoscience*, *10*(5), 333-337.

Agard, P., Plunder, A., Angiboust, S., Bonnet, G., & Ruh, J. (2018). The subduction plate interface: rock record and mechanical coupling (from long to short timescales). *Lithos*, *320*, 537-566.

Angiboust, S., Agard, P., Yamato, P., & Raimbourg, H. (2012). Eclogite breccias in a subducted ophiolite: A record of intermediate-depth earthquakes?. *Geology*, *40*(8), 707-710.

Angiboust, S., Pettke, T., De Hoog, J. C., Caron, B., & Oncken, O. (2014). Channelized fluid flow and eclogite-facies metasomatism along the subduction shear zone. *Journal of petrology*, *55*(5), 883-916.

Angiboust, S., Kirsch, J., Oncken, O., Glodny, J., Monié, P., & Rybacki, E. (2015). Probing the transition between seismically coupled and decoupled segments along an ancient subduction interface. *Geochemistry, Geophysics, Geosystems*, *16*(6), 1905-1922.

995 Angiboust, S., Glodny, J., Cambeses, A., Raimondo, T., Monié, P., Popov, M., & Garcia-Casco, A. (2021).
996 Drainage of subduction interface fluids into the forearc mantle evidenced by a pristine jadeitite
997 network (Polar Urals). *Journal of Metamorphic Geology*. *39*(4), 473-500.
998 Antriasian, A., Harris, R. N., Tréhu, A. M., Henrys, S. A., Phrampus, B. J., Lauer, R., ... & Barker, D. (2019).
999 Thermal regime of the northern Hikurangi margin, New Zealand. *Geophysical Journal International*,
1000 *216*(2), 1177-1190.
1001 Audet, P., & Kim, Y. (2016). Teleseismic constraints on the geological environment of deep episodic slow
1002 earthquakes in subduction zone forearcs: A review. *Tectonophysics*, *670*, 1-15.
1003 Austrheim, H., & Boundy, T. M. (1994). Pseudotachylytes generated during seismic faulting and
1004 eclogitization of the deep crust. *Science*, 265(5168), 82-83.
1005 Austrheim, H., & Andersen, T. B. (2004). Pseudotachylytes from Corsica: fossil earthquakes from a
1006 subduction complex. *Terra nova*, *16*(4), 193-197.
1007 Bachmann, F., Hielscher, R., & Schaeben, H. (2010). Texture analysis with MTEX–free and open source
1008 software toolbox. In Solid State Phenomena (Vol. 160, pp. 63-68). *Trans Tech Publications Ltd*.
1009 Bachmann, F., Hielscher, R., & Schaeben, H. (2011). Grain detection from 2d and 3d EBSD data—
1010 Specification of the MTEX algorithm. *Ultramicroscopy*, 111(12), 1720-1733.
1011 Batanova, V. G., Belousov, I. A., Savelieva, G. N., & Sobolev, A. V. (2011). Consequences of channelized
1012 and diffuse melt transport in supra-subduction zone mantle: evidence from the Voykar ophiolite
1013 (Polar Urals). *J. Petrol*. 52(12), 2483-2521.
1014 Bebout, G. E. (2007). Metamorphic chemical geodynamics of subduction zones. *Earth and Planetary*
1015 *Science Letters*, 260(3-4), 373-393.
1016 Beccaluva, L., Bellia, S., Coltorti, M., Dengo, G., Giunta, G., Mendez, J., Romero, J., Rotolo, S. and Siena,
1017 F., 1995. The northwestern border of the Caribbeanplate in Guatemala: New geological and
1018 petrological data on the Motagua ophiolitic belt. Ofioliti, 20, 1-15.
1019 Bleek, A.W.G (1908). Jadeite in the Kachin Hills, Upper Burma. *Records of the Geological Survey India*,
1020 36(4), 254-285.
1021 Bostock, M. G. (2013). The Moho in subduction zones. *Tectonophysics*, *609*, 547-557.
1022 Bouchon, M., Marsan, D., Jara, J., Socquet, A., Campillo, M., & Perfettini, H. (2018). Suspected deep
1023 interaction and triggering between giant earthquakes in the Chilean subduction zone. *Geophysical*
1024 *Research Letters*, *45*(11), 5454-5460.
1025 Brueckner, H. K., Lallemant, H. G. A., Sisson, V. B., Harlow, G. E., Hemming, S. R., Martens, U., ... &
1026 Sorensen, S. S. (2009). Metamorphic reworking of a high pressure–low temperature mélange along

1027 the Motagua fault, Guatemala: a record of Neocomian and Maastrichtian transpressional tectonics.
1028 *Earth and Planetary Science Letters*, *284*(1-2), 228-235.
1029 Bull, K. F., & McPhie, J. (2007). Fiamme textures in volcanic successions: Flaming issues of definition and
1030 interpretation. *Journal of Volcanology and Geothermal Research*, *164*(4), 205-216.
1031 Cárdenas-Párraga, J., García-Casco, A., Harlow, G. E., Blanco-Quintero, I. F., Agramonte, Y. R., & Kröner,
1032 A. (2012). Hydrothermal origin and age of jadeitites from Sierra del Convento Mélange (Eastern
1033 Cuba). *European Journal of Mineralogy*, *24*(2), 313-331.
1034 Chang, Y., Warren, L. M., Zhu, L., & Prieto, G. A. (2019). Earthquake focal mechanisms and stress field for
1035 the intermediate-depth Cauca cluster, Colombia. *Journal of Geophysical Research: Solid Earth*,
1036 124(1), 822-836.
1037 Chen, Y., Huang, F., Shi, G. H., Wu, F. Y., Chen, X., Jin, Q. Z., ... & Nyunt, T. T. (2018). Magnesium isotope
1038 composition of subduction zone fluids as constrained by jadeitites from Myanmar. *Journal of*
1039 *Geophysical Research: Solid Earth*, *123*(9), 7566-7585.
1040 Chhiber HL. 1934. *The Mineral Resources of Burma*. London: MacMillan
1041 Cox, S. F., & Munroe, S. M. (2016). Breccia formation by particle fluidization in fault zones: implications
1042 for transitory, rupture-controlled fluid flow regimes in hydrothermal systems. *American Journal of*
1043 *Science*, *316*(3), 241-278.
1044 Davey, F. J., & Ristau, J. (2011). Fore-arc mantle wedge seismicity under northeast New Zealand.
1045 *Tectonophysics*, *509*(3-4), 272-279.
1046 Deschamps, F., Guillot, S., Godard, M., Chauvel, C., Andreani, M., & Hattori, K. (2010). In situ
1047 characterization of serpentinites from forearc mantle wedges: timing of serpentinization and
1048 behavior of fluid-mobile elements in subduction zones. *Chemical Geology*, *269*(3-4), 262-277.
1049 Dessa, J. X., Klingelhoefer, F., Graindorge, D., André, C., Permana, H., Gutscher, M. A., ... & SUMATRA-
1050 OBS Scientific Team. (2009). Megathrust earthquakes can nucleate in the forearc mantle: Evidence
1051 from the 2004 Sumatra event. *Geology*, *37*(7), 659-662.
1052 Dobretsov, N. L., & N. V. Sobolev (1984). Glaucophane schists and eclogites in the folded systems of
1053 northern Asia. *Ofioliti*, 9. 401-424.
1054 Dobretsov, N. L., & Ponomareva, L. G. (1968). Comparative characteristics of jadeite and associated rocks
1055 from Polar Ural and Prebalkhash region. *International Geology Review*, 10(3), 247-279.
1056 Doglioni, C., Tonarini, S., & Innocenti, F. (2009). Mantle wedge asymmetries and geochemical signatures
1057 along W-and E–NE-directed subduction zones. *Lithos*, *113*(1-2), 179-189.

1058 Dressler, B. O., & Reimold, W. U. (2001). Terrestrial impact melt rocks and glasses. *Earth-Science*
1059 *Reviews*, *56*(1-4), 205-284.
1060 Endo, S., Wallis, S. R., Tsuboi, M., Torres De León, R., & Solari, L. A. (2012). Metamorphic evolution of
1061 lawsonite eclogites from the southern Motagua fault zone, Guatemala: insights from phase
1062 equilibria and Raman spectroscopy. *Journal of Metamorphic Geology*, *30*(2), 143-164.
1063 Escartin, J., Hirth, G., & Evans, B. (2001). Strength of slightly serpentinized peridotites: Implications for
1064 the tectonics of oceanic lithosphere. *Geology*, *29*(11), 1023-1026.
1065 Fishman, A.M. (2006): Gems in the north Ural and Timan. *Geoprint*, Syktyvkar, 88 p. (in Russian).
1066 Flores, K. E., Skora, S., Martin, C., Harlow, G. E., Rodríguez, D., & Baumgartner, P. O. (2015). Metamorphic
1067 history of riebeckite-and aegirine-augite-bearing high-pressure–low-temperature blocks within the
1068 Siuna Serpentinite Mélange, northeastern Nicaragua. *International Geology Review*, *57*(5-8), 943-
1069 977.
1070 Flores, K. E., Martens, U. C., Harlow, G. E., Brueckner, H. K., & Pearson, N. J. (2013). Jadeitite formed
1071 during subduction: In situ zircon geochronology constraints from two different tectonic events
1072 within the Guatemala Suture Zone. *Earth and Planetary Science Letters*, *371*, 67-81.
1073 Frank, W. B., Shapiro, N. M., Husker, A. L., Kostoglodov, V., Bhat, H. S., & Campillo, M. (2015). Along-fault
1074 pore-pressure evolution during a slow-slip event in Guerrero, Mexico. *Earth and Planetary Science*
1075 *Letters*, 413, 135-143.
1076 Franz, L., Sun, T. T., Hänni, H. A., de Capitani, C., Thanasuthipitak, T., Atichat, W., ... & Capitani, C. D.
1077 (2014). A comparative study of jadeite, omphacite and kosmochlor jades from Myanmar, and
1078 suggestions for a practical nomenclature. *J. Gemmol*, 34, 210-229.
1079 Fu, Y., & Freymueller, J. T. (2013). Repeated large slow slip events at the southcentral Alaska subduction
1080 zone. *Earth and Planetary Science Letters*, *375*, 303-311.
1081 García-Casco, A. (2007). Magmatic paragonite in trondhjemites from the Sierra del Convento mélange,
1082 Cuba. *American Mineralogist*, 92(7), 1232-1237.
1083 García-Casco, A., Vega, A. R., Párraga, J. C., Iturralde-Vinent, M. A., Lázaro, C., Quintero, I. B., ... & Torres-
1084 Roldán, R. L. (2009). A new jadeitite jade locality (Sierra del Convento, Cuba): first report and some
1085 petrological and archeological implications. Contributions to Mineralogy and Petrology, 158(1), 1.
1086 Gendron, F., Smith, D. C., & Gendron-Badou, A. (2002). Discovery of jadeite-jade in Guatemala confirmed
1087 by non-destructive Raman microscopy. *Journal of Archaeological Science*, 29(8), 837-851.
1088 Gerya, T. V., Stöckhert, B., & Perchuk, A. L. (2002). Exhumation of high-pressure metamorphic rocks in a
1089 subduction channel: A numerical simulation. *Tectonics*, 21(6), 6-1.

1090 Glodny, J., Austrheim, H., Molina, J. F., Rusin, A. I., & Seward, D. (2003). Rb/Sr record of fluid-rock
1091 interaction in eclogites: The Marun-Keu complex, Polar Urals, Russia. *Geochimica et Cosmochimica*
1092 *Acta*, *67*(22), 4353-4371.
1093 Godard, G., & van Roermund, H. L. (1995). Deformation-induced clinopyroxene fabrics from eclogites.
1094 *Journal of Structural Geology*, 17(10), 1425-1443.
1095 Goffé, B., C. Rangin, and H. Maluski (2002), Jade and associated rocks from the jade Mines area,
1096 Northern Myanmar as record of a polyphased high pressure metamorphism. Himalaya–Karakoram–
1097 Tibet Workshop meeting (abstract) ,*J. Asian Earth Sc*i.,20,16–17.
1098 Guillot, S., Hattori, K., Agard, P., Schwartz, S., & Vidal, O. (2009). Exhumation processes in oceanic and
1099 continental subduction contexts: a review. *Subduction zone geodynamics*, 175-205.
1100 Hacker, B. R., Abers, G. A., & Peacock, S. M. (2003). Subduction factory 1. Theoretical mineralogy,
1101 densities, seismic wave speeds, and H2O contents. *Journal of Geophysical Research: Solid Earth*,
1102 108(B1).
1103 Halpaap, F., Rondenay, S., Perrin, A., Goes, S., Ottemöller, L., Austrheim, H., ... & Eeken, T. (2019).
1104 Earthquakes track subduction fluids from slab source to mantle wedge sink. *Science Advances*, *5*(4),
1105 eaav7369.
1106 Hao, M., Pierotti, C. E., Tkachev, S., Prakapenka, V., & Zhang, J. S. (2019). The single-crystal elastic
1107 properties of the jadeite-diopside solid solution and their implications for the composition-
1108 dependent seismic properties of eclogite, *American Mineralogist*, *104*(7), 1016-1021.
1109 Harlow, G. E., Hemming, S. R., Lallemant, H. G. A., Sisson, V. B., & Sorensen, S. S. (2004). Two high-
1110 pressure–low-temperature serpentinite-matrix mélange belts, Motagua fault zone, Guatemala: a
1111 record of Aptian and Maastrichtian collisions. *Geology*, *32*(1), 17-20.
1112 Harlow, G. E., & Sorensen, S. S. (2005). Jade (nephrite and jadeitite) and serpentinite: metasomatic
1113 connections. *International Geology Review*, *47*(2), 113-146.
1114 Harlow, G. E., Sisson, V. B., Tsujimori, T., Sorensen, S. S., & Brueckner, H. K. (2008). P–T conditions of
1115 eclogite/garnet–amphibolite from serpentinite mélanges along the Motagua fault zone, Guatemala.
1116 *Abs. Ann. Meet. Geol. Soc. Amer.: http://acs. confex. com/crops/2008am/webprogram/Paper50090.*
1117 *html*.
1118 Harlow, G. E., Sisson, V. B., & Sorensen, S. S. (2011). Jadeitite from Guatemala: new observations and
1119 distinctions among multiple occurrences. *Geologica Acta*, *9*(3-4), 0363-387.
1120 Harlow, G. E., Tsujimori, T., & Sorensen, S. S. (2015). Jadeitites and plate tectonics. *Annual Review of*
1121 *Earth and Planetary Sciences*, *43*, 105-138.

1122 Harlow, G. E., Flores, K. E., & Marschall, H. R. (2016). Fluid-mediated mass transfer from a
1123 paleosubduction channel to its mantle wedge: evidence from jadeitite and related rocks from the
1124 Guatemala Suture Zone. *Lithos*, *258*, 15-36.
1125 Hawthorne, F. C., & Oberti, R. (2007). Classification of the amphiboles. *Reviews in Mineralogy and*
1126 *Geochemistry*, *67*(1), 55-88.
1127 Hellstrom, J., C. Paton, J. Woodhead, and J. Hergt (2008), Iolite: software for spatially resolved LA-(quad
1128 and MC) ICPMS analysis, *Mineralogical Association of Canada short course series*, 40, 343-348.
1129 Hermann, J., Spandler, C., Hack, A., & Korsakov, A. V. (2006). Aqueous fluids and hydrous melts in high-
1130 pressure and ultra-high pressure rocks: implications for element transfer in subduction zones.
1131 *Lithos*, *92*(3-4), 399-417.
1132 Hertgen, S., Yamato, P., Morales, L. F., & Angiboust, S. (2017). Evidence for brittle deformation events at
1133 eclogite-facies PT conditions (example of the Mt. Emilius klippe, Western Alps). *Tectonophysics*, *706*,
1134 1-13.
1135 Hertwig, A., McClelland, W. C., Kitajima, K., Schertl, H. P., Maresch, W. V., Stanek, K., ... & Sergeev, S. A.
1136 (2016). Inherited igneous zircons in jadeitite predate high-pressure metamorphism and jadeitite
1137 formation in the Jagua Clara serpentinite mélange of the Rio San Juan Complex (Dominican
1138 Republic). *Contributions to Mineralogy and Petrology*, 171(5), 48.
1139 Hilairet, N., Reynard, B., Wang, Y., Daniel, I., Merkel, S., Nishiyama, N., & Petitgirard, S. (2007). High-
1140 pressure creep of serpentine, interseismic deformation, and initiation of subduction. *Science*,
1141 *318*(5858), 1910-1913.
1142 Horn, C., Bouilhol, P., & Skemer, P. (2020). Serpentinization, deformation, and seismic anisotropy in the
1143 subduction mantle wedge. *Geochemistry, Geophysics, Geosystems*, *21*(4), e2020GC008950.
1144 Huang, J., Hao, J., Huang, F., & Sverjensky, D. (2019). Mobility of chromium in high temperature crustal
1145 and upper mantle fluids. *Geochemical Perspectives Letters*, 12, 1-6.
1146 Hussong, D. M. (1981). Tectonic processes and the history of the Mariana arc: a synthesis of the results
1147 of Deep Sea Drilling Project Leg 60. *Initial reports of the deep sea drilling project*, 60, 909-929.
1148 Hyndman, R. D., & Peacock, S. M. (2003). Serpentinization of the forearc mantle. *Earth and Planetary*
1149 *Science Letters*, 212(3-4), 417-432.
1150 Hyppolito, T., Cambeses, A., Angiboust, S., Raimondo, T., García-Casco, A., & Juliani, C. (2018).
1151 Rehydration of eclogites and garnet-replacement processes during exhumation in the amphibolite
1152 facies. *Geological Society, London, Special Publications*, 478, SP478.473. doi:10.1144/sp478.3.

1153 Jochum, K. P., et al. (2011a), Determination of Reference Values for NIST SRM 610–617 Glasses Following
1154 ISO Guidelines, *Geostandards and Geoanalytical Research*, 35(4), 397-429.
1155 Jochum, K.P., Wilson, S.A., Abouchami, W., Amini, M., Chmeleff, J., Eisenhauer, A., Hegner, E., Iaccheri,
1156 L.M., Kieffer, B., Krause, J., McDonough, W.F., Mertz-Kraus, R., Raczek, I., Rudnick, R.L., Scholz, D.,
1157 Steinhoefel, G., Stoll, B., Stracke, A., Tonarini, S., Weis, D., Weis, U. & Woodhead, J.D. (2011b). GSD-
1158 1G and MPI-DING Reference Glasses for In Situ and Bulk Isotopic Determination. *Geostandards and*
1159 *Geoanalytical Research*, 35, 193-226, doi: 10.1111/j.1751-908X.2010.00114.x.
1160 Kawamoto, T., Hertwig, A., Schertl, H. P., & Maresch, W. V. (2018). Fluid inclusions in jadeitite and
1161 jadeite-rich rock from serpentinite mélanges in northern Hispaniola: Trapped ambient fluids in a
1162 cold subduction channel. *Lithos*, 308, 227-241.
1163 Kazak, A.P., Dobretsov, N.L., Moldavantsev, J.E. (1976). Glaucophane schists, jadeitites, vesuvianites and
1164 nephrites of the Rai-Iz ultramafic massif. *Geology and Geophysics* (in Russian), 2, 60-66.
1165 Kepezhinskas, P. K., Defant, M. J., & Drummond, M. S. (1995). Na-metasomatism in the island-arc mantle
1166 by slab melt—peridotite interaction: evidence from mantle xenoliths in the North Kamchatka Arc.
1167 *Journal of Petrology*, 36(6), 1505-1527.
1168 Keppler, R., Stipp, M., Behrmann, J. H., Ullemeyer, K., & Heidelbach, F. (2016). Deformation inside a
1169 paleosubduction channel–Insights from microstructures and crystallographic preferred orientations
1170 of eclogites and metasediments from the Tauern Window, Austria. *Journal of Structural Geology*, 82,
1171 60-79.
1172 Keppler, R. (2018). Crystallographic preferred orientations in eclogites–A review. *Journal of Structural*
1173 *Geology*, 115, 284-296.
1174 Kirkpatrick, J. D., & Rowe, C. D. (2013). Disappearing ink: How pseudotachylytes are lost from the rock
1175 record. *Journal of Structural Geology*, *52*, 183-198.
1176 Konovalov A.L. & Sergeev S.S. (2015). About the age of zircons from jadeitite ultrabasite array of Syomke
1177 in the zone of the Main Uralian fault (the Polar Urals). *Regionalnaya geologiya i metallogeniya*. 64,
1178 41–47. (In Russian).
1179 Kuznetsov, Y. V., Kuznetsova, N. A., & Tsyutskiy, S. S. (1986). Features of jadeite mineralization in the
1180 Pus'yerka deposit (Polar Urals). *International Geology Review*, 28(9), 1096-1101.
1181 Lázaro, C., Blanco-Quintero, I. F., Marchesi, C., Bosch, D., Rojas-Agramonte, Y., & García-Casco, A. (2011).
1182 The imprint of subduction fluids on subducted MORB-derived melts (Sierra del Convento Mélange,
1183 Cuba). *Lithos*, 126(3-4), 341-354.

1184 Liu, W., Zhang, J., Cao, Y., & Jin, Z. (2020). Geneses of two contrasting antigorite crystal preferred
1185 orientations and their implications for seismic anisotropy in the forearc mantle. *Journal of*
1186 *Geophysical Research: Solid Earth*, *125*(9), e2020JB019354.
1187 Locatelli, M., Verlaguet, A., Agard, P., Federico, L., & Angiboust, S. (2018). Intermediate-depth
1188 brecciation along the subduction plate interface (Monviso eclogite, W. Alps). *Lithos*, *320*, 378-402.
1189 Luo, H., & Wang, K. (2021). Postseismic geodetic signature of cold forearc mantle in subduction zones.
1190 *Nature Geoscience*, 1-6.
1191 Magloughlin, J. F. (1992). Microstructural and chemical changes associated with cataclasis and frictional
1192 melting at shallow crustal levels: the cataclasite-pseudotachylyte connection. *Tectonophysics*,
1193 *204*(3-4), 243-260.
1194 Makeyev, A.B. (1992) Mineralogy of alpine-type ultramafics in the Ural. Nauka, St. Petersburg. 195 p. (in
1195 Russian).

1196 Maruyama, S., & Liou, J. G. (1988). Petrology of Franciscan metabasites along the jadeite-glaucophane
1197 type facies series, Cazadero, California. *Journal of Petrology*, 29(1), 1-37.

1198 Melosh, B. L., Rowe, C. D., Smit, L., Groenewald, C., Lambert, C. W., & Macey, P. (2014). Snap, Crackle,
1199 Pop: Dilational fault breccias record seismic slip below the brittle–plastic transition. *Earth and*
1200 *Planetary Science Letters*, *403*, 432-445.
1201 Menant, A., Angiboust, S., Monié, P., Oncken, O., & Guigner, J. M. (2018). Brittle deformation during
1202 Alpine basal accretion and the origin of seismicity nests above the subduction interface. *Earth and*
1203 *Planetary Science Letters*, *487*, 84-93.
1204 Meng, F., Yang, H. J., Makeyev, A. B., Ren, Y., Kulikova, K. V., & Bryanchaninova, N. I. (2016). Jadeitite in
1205 the Syum-Keu ultramafic complex from Polar Urals, Russia: insights into fluid activity in subduction
1206 zones. *European Journal of Mineralogy*, 28(6), 1079-1097.
1207 Meng, F., Makeyev, A. B., & Yang, J. (2011). Zircon U–Pb dating of jadeitite from the Syum-Keu ultramafic
1208 complex, Polar Urals, Russia: constraints for subduction initiation. *Journal of Asian Earth Sciences*,
1209 *42*(4), 596-606.
1210 Mével, C., & Kienast, J. R. (1986). Jadeite-kosmochlor solid solution and chromian sodic amphiboles in
1211 jadeitites and associated rocks from Tawmaw (Burma). *Bulletin de Minéralogie*, *109*(6), 617-633.
1212 Morimoto, N. (1989). Nomenclature of pyroxenes. *Mineralogical Journal*, *14*(5), 198-221.

1213 Morishita, T., Arai, S., & Ishida, Y. (2007). Trace element compositions of jadeite (+ omphacite) in
1214 jadeitites from the Itoigawa-Ohmi district, Japan: Implications for fluid processes in subduction
1215 zones. *Island Arc*, 16(1), 40-56.
1216 Muñoz-Montecinos, J., Angiboust, S., Garcia-Casco, A., Glodny, J., & Bebout, G. (2021b). Episodic
1217 hydrofracturing and large-scale flushing along deep subduction interfaces: Implications for fluid
1218 transfer and carbon recycling (Zagros Orogen, southeastern Iran). *Chemical Geology*, 571, 120173.
1219 Muñoz-Montecinos J, Angiboust S, Garcia-Casco A, (2021a) Blueschist-facies paleo-earthquakes in a
1220 serpentinite channel enlighten seismogenesis in Mariana-type subduction margins, Accepted (*Earth
1221 and planetary science letters*)**.**
1222 Nakajima, J., & Uchida, N. (2018). Repeated drainage from megathrusts during episodic slow slip. *Nature
1223 Geoscience*, *11*(5), 351-356.
1224 Nyunt, T. T., Massonne, H. J., & Sun, T. T. (2017). Jadeitite and other high-pressure metamorphic rocks
1225 from the Jade Mines Belt, Tawmaw area, Kachin State, northern Myanmar. *Geological Society,
1226 London, Memoirs*, *48*(1), 295-315.
1227 Nyunt, T. T. (2009). Petrological and geochemical contribution to the origin of jadeitite and associated
1228 rocks of the Tawmaw Area, Kachin State, Myanmar. Stuttgart PhD thesis.
1229 Obara, K., & Kato, A. (2016). Connecting slow earthquakes to huge earthquakes. *Science*, 353(6296), 253-
1230 257.
1231 Oberti, R., Boiocchi, M., Hawthorne, F. C., Ball, N. A., & Harlow, G. E. (2015). Eckermannite revised: The
1232 new holotype from the Jade Mine Tract, Myanmar—crystal structure, mineral data, and hints on the
1233 reasons for the rarity of eckermannite. *American Mineralogist*, 100(4), 909-914.
1234 Oncken O, Angiboust S, Dresen G, Slow slip in subduction zones: Reconciling deformation fabrics with
1235 instrumental observations and laboratory results, In revision**.**
1236 Ortega-Gutiérrez, F., Solari, L. A., Ortega-Obregon, C., Elias-Herrera, M., Martens, U., Moran-Ical, S., ... &
1237 Schaaf, P. (2007). The Maya-Chortís boundary: a tectonostratigraphic approach. *International
1238 Geology Review*, *49*(11), 996-1024.
1239 Orzol, J., Stöckhert, B., Trepmann, C. A., & Rummel, F. (2006). Experimental deformation of synthetic wet
1240 jadeite aggregates. *Journal of Geophysical Research: Solid Earth*, *111*(B6).
1241 Paton, C., J. Hellstrom, B. Paul, J. Woodhead, and J. Hergt (2011), Iolite: Freeware for the visualisation
1242 and processing of mass spectrometric data, *Journal of Analytical Atomic Spectrometry*, 26(12), 2508-
1243 2518.

1244 Peacock, S. M. (2003). Thermal structure and metamorphic evolution of subducting slabs. *Geophysical*
1245 *Monograph-American Geophysical Union*, *138*, 7-22.
1246 Pearce, N. J. G., W. T. Perkins, J. A. Westgate, M. P. Gorton, S. E. Jackson, C. R. Neal, and S. P. Chenery
1247 (1997), A compilation of new and published major and trace element data for NIST SRM 610 and
1248 NIST SRM 612 glass reference materials, Geostandards Newsletter - *Journal of Geostandards and*
1249 *Geoanalysis*, 21(1), 115-144.
1250 Pfiffner, O. A., & Ramsay, J. G. (1982). Constraints on geological strain rates: arguments from finite strain
1251 states of naturally deformed rocks. *Journal of Geophysical Research: Solid Earth*, *87*(B1), 311-321.
1252 Philippot, P., & van Roermund, H. L. (1992). Deformation processes in eclogitic rocks: evidence for the
1253 rheological delamination of the oceanic crust in deeper levels of subduction zones. *Journal of*
1254 *structural geology*, 14(8-9), 1059-1077.
1255 Prigent, C., Guillot, S., Agard, P., Lemarchand, D., Soret, M., & Ulrich, M. (2018). Transfer of subduction
1256 fluids into the deforming mantle wedge during nascent subduction: Evidence from trace elements
1257 and boron isotopes (Semail ophiolite, Oman). *Earth and Planetary Science Letters*, 484, 213-228.
1258 Putnis, A., & Austrheim, H. (2013). Mechanisms of metasomatism and metamorphism on the local
1259 mineral scale: The role of dissolution-reprecipitation during mineral re-equilibration. In
1260 *Metasomatism and the chemical transformation of rock* (pp. 141-170). Springer, Berlin, Heidelberg.
1261 Raimondo, T., Payne, J., Wade, B., Lanari, P., Clark, C., & Hand, M. (2017). Trace element mapping by LA-
1262 ICP-MS: assessing geochemical mobility in garnet. *Contributions to mineralogy and petrology*,
1263 *172*(4), 17.
1264 Reynard, B. (2013). Serpentine in active subduction zones. *Lithos*, *178*, 171-185.
1265 Ridd, M. F., Crow, M. J., & Morley, C. K. (2019). The role of strike-slip faulting in the history of the
1266 Hukawng Block and the Jade Mines Uplift, Myanmar. *Proceedings of the Geologists' Association*,
1267 *130*(2), 126-141.
1268 Rowe, C. D., Meneghini, F., & Moore, J. C. (2011). Textural record of the seismic cycle: Strain-rate
1269 variation in an ancient subduction thrust. *Geological Society, London, Special Publications*, *359*(1),
1270 77-95.
1271 Savelieva, G. N., Sharaskin, A. Y., Saveliev, A. A., et al. (2002). Ophiolites and zoned mafic–ultramafic
1272 massifs of the Urals: a comparative analysis and some tectonic implications. *Mountain building in*
1273 *the Uralides*, 135-153.

Savelieva, G. N., & Suslov, P. V. (2014). Structure and composition of mantle peridotites at the boundary with crustal complexes of ophiolites in the Syumkeu massif, Polar Urals. *Geotectonics*, *48*(5), 347-358.

Savelieva, G. N., Batanova, V. G., & Sobolev, A. V. (2016). Pyroxene–Cr-spinel exsolution in mantle lherzolites of the Syum-Keu ophiolite massif (Arctic Urals). *Russian Geology and Geophysics*, *57*(10), 1419-1436.

Scambelluri, M., Cannaò, E., & Gilio, M. (2019). The water and fluid-mobile element cycles during serpentinite subduction. A review. *European Journal of Mineralogy*, 31(3), 405-428.

Schertl, H. P., Maresch, W. V., Stanek, K. P., Hertwig, A., Krebs, M., Baese, R., & Sergeev, S. S. (2012). New occurrences of jadeitite, jadeite quartzite and jadeite-lawsonite quartzite in the Dominican Republic, Hispaniola: petrological and geochronological overview. *European Journal of Mineralogy*, *24*(2), 199-216.

Searle, M. P., Noble, S. R., Cottle, J. M., Waters, D. J., Mitchell, A. H. G., Hlaing, T., & Horstwood, M. S. A. (2007). Tectonic evolution of the Mogok metamorphic belt, Burma (Myanmar) constrained by U-Th-Pb dating of metamorphic and magmatic rocks. *Tectonics*, *26*(3).

Shi, G. H., Cui, W. Y., Tropper, P., Wang, C. Q., Shu, G. M., & Yu, H. (2003). The petrology of a complex sodic and sodic–calcic amphibole association and its implications for the metasomatic processes in the jadeitite area in northwestern Myanmar, formerly Burma. *Contributions to Mineralogy and Petrology*, *145*(3), 355-376.

Shi, G. H., Jiang, N., Liu, Y., Wang, X., Zhang, Z. Y., & Xu, Y. J. (2009a). Zircon Hf isotope signature of the depleted mantle in the Myanmar jadeitite: implications for Mesozoic intra-oceanic subduction between the Eastern Indian Plate and the Burmese Platelet. *Lithos*, *112*(3-4), 342-350.

Shi, G., Wang, X., Chu, B., & Cui, W. (2009b). Jadeite jade from Myanmar: its texture and gemmological implications. *The journal of gemmology and proceedings of the Gemmological Association of Great Britain*, 31(5), 185.

Shi, G., Harlow, G. E., Wang, J., Wang, J., Ng, E., Wang, X., ... & Cui, W. (2012). Mineralogy of jadeitite and related rocks from Myanmar: a review with new data. *European Journal of Mineralogy*, 24(2), 345-370.

Shigeno, M., Mori, Y., Shimada, K., & Nishiyama, T. (2012). Jadeitites with metasomatic zoning from the Nishisonogi metamorphic rocks, western Japan: fluid–tectonic block interaction during exhumation. *European Journal of Mineralogy*, 24(2), 289-311.

1305 Shmelev, V. R. (2011). Mantle ultrabasites of ophiolite complexes in the Polar Urals: petrogenesis and
1306 geodynamic environments. *Petrology*, *19*(6), 618-640.
1307 Sibson, R. H. (1986). Brecciation processes in fault zones: inferences from earthquake rupturing. *Pure*
1308 *and Applied Geophysics*, *124*(1), 159-175.
1309 Sibson, R. H. (1989). Earthquake faulting as a structural process. *Journal of structural geology*, *11*(1-2), 1-
1310 14.
1311 Sibson, R. H., Toy, V. G., Abercrombie, R., & McGarr, A. (2006). The habitat of fault-generated
1312 pseudotachylyte: Presence vs. absence of friction-melt. *GEOPHYSICAL MONOGRAPH-AMERICAN*
1313 *GEOPHYSICAL UNION*, *170*, 153.
1314 Snoke, A. W., Tullis, J., & Todd, V. R. (Eds.). (2014). *Fault-related rocks: a photographic atlas* (Vol. 410).
1315 Princeton University Press.
1316 Sorensen, S., Harlow, G. E., & Rumble, D. (2006). The origin of jadeitite-forming subduction-zone fluids:
1317 CL-guided SIMS oxygen-isotope and trace-element evidence. *American Mineralogist*, *91*(7), 979-996.
1318 Sorensen, S. S., Sisson, V. B., Harlow, G. E., & Avé Lallemant, H. G. (2010). Element residence and
1319 transport during subduction-zone metasomatism: evidence from a jadeitite-serpentinite contact,
1320 Guatemala. *International Geology Review*, *52*(9), 899-940.
1321 Soret, M., Agard, P., Dubacq, B., Vitale-Brovarone, A., Monie, P., Chauvet, A., ... & Villemant, B. (2016).
1322 Strain localization and fluid infiltration in the mantle wedge during subduction initiation: Evidence
1323 from the base of the New Caledonia ophiolite. *Lithos*, 244, 1-19.
1324 Spandler, C., & Pirard, C. (2013). Element recycling from subducting slabs to arc crust: A review. *Lithos*,
1325 170, 208-223.
1326 Swanson, M. T. (1992). Fault structure, wear mechanisms and rupture processes in pseudotachylyte
1327 generation. *Tectonophysics*, *204*(3-4), 223-242.
1328 Sychev, S. N., & Kulikova, K. V. (2012). Structural evolution of the Main Ural Fault Zone in the western
1329 framework of the Voikar-Synya ophiolite massif. *Geotectonics*, *46*(6), 427-434.
1330 Syracuse, E. M., van Keken, P. E., & Abers, G. A. (2010). The global range of subduction zone thermal
1331 models. *Physics of the Earth and Planetary Interiors*, *183*(1-2), 73-90.
1332 Takahashi, N., Tsujimori, T., Kayama, M., & Nishido, H. (2017). Cathodoluminescence petrography of P–
1333 type jadeitites from the New Idria serpentinite body, California. *Journal of Mineralogical and*
1334 *Petrological Sciences*, *112*(5), 291-299.

Torres-Roldan, R. L., Garcia-Casco, A., & Garcia-Sanchez, P. A. (2000). CSpace: An integrated workplace for the graphical and algebraic analysis of phase assemblages on 32-bit Wintel platforms. *Computers & Geosciences*, *26*(7), 779-793.

Tsujimori, T., & Harlow, G. E. (2012). Petrogenetic relationships between jadeitite and associated high-pressure and low-temperature metamorphic rocks in worldwide jadeitite localities: a review. *European Journal of Mineralogy*, *24*(2), 371-390.

Tsujimori, T., Liou, J. G., & Coleman, R. G. (2004, November). Comparison of two contrasting eclogites from the Motagua fault zone, Guatemala: southern lawsonite eclogite versus northern zoisite eclogite. In *Geological Society of America Abstracts with Programs* (Vol. 36, No. 5, p. 136).

Uchida, N., Kirby, S. H., Okada, T., Hino, R., & Hasegawa, A. (2010). Supraslab earthquake clusters above the subduction plate boundary offshore Sanriku, northeastern Japan: Seismogenesis in a graveyard of detached seamounts?. *Journal of Geophysical Research: Solid Earth*, *115*(B9).

Udovkina, N.G. (1971). Eclogites of Polar Urals Nauka, Moscow (in Russian).

Ulrich, S., & Mainprice, D. (2005). Does cation ordering in omphacite influence development of lattice-preferred orientation?. *Journal of Structural Geology*, 27(3), 419-431.

Wang, K., Huang, T., Tilmann, F., Peacock, S. M., & Lange, D. (2020). Role of Serpentinized Mantle Wedge in Affecting Megathrust Seismogenic Behavior in the Area of the 2010 M= 8.8 Maule Earthquake. Geophysical Research Letters, 47(22), e2020GL090482.

White, L., Rawlinson N., Lister G., Tanner D., Macpherson C., and Morgan J. (2016). Pulses of earthquake activity in the mantle wedge track the route of slab fluid ascent. EGU General Assembly Conference Abstracts, 18. 2016.

Whitney, D. L., & Evans, B. W. (2010). Abbreviations for names of rock-forming minerals. *American mineralogist*, *95*(1), 185-187.

Woodcock, N. H., Dickson, J. A. D., & Tarasewicz, J. P. T. (2007). Transient permeability and reseal hardening in fault zones: evidence from dilation breccia textures. *Geological Society, London, Special Publications*, *270*(1), 43-53.

Woodcock, N. H., & Mort, K. (2008). Classification of fault breccias and related fault rocks. *Geological Magazine*, *145*(3), 435-440.

Woodhead, J. D., J. Hellstrom, J. M. Hergt, A. Greig, and R. Maas (2007). Isotopic and Elemental Imaging of Geological Materials by Laser Ablation Inductively Coupled Plasma-Mass Spectrometry, *Geostandards and Geoanalytical Research*, 31(4), 331-343.

Yu, Z., & Zhao, D. (2020). Seismic evidence for water transportation in the forearc off Northern Japan. *Journal of Geophysical Research: Solid Earth*, *125*(4), e2019JB018600.

Yui, T. F., Fukoyama, M., Iizuka, Y., Wu, C. M., Wu, T. W., Liou, J. G., & Grove, M. (2013). Is Myanmar jadeitite of Jurassic age? A result from incompletely recrystallized inherited zircon. *Lithos*, *160*, 268-282.

Yui, T. F., Maki, K., Wang, K. L., Lan, C. Y., Usuki, T., Iizuka, Y., ... & Grove, M. (2012). Hf isotope and REE compositions of zircon from jadeitite (Tone, Japan and north of the Motagua fault, Guatemala): implications on jadeitite genesis and possible protoliths. *European Journal of Mineralogy*, *24*(2), 263-275.

Zhang, J., Green II, H. W., & Bozhilov, K. N. (2006). Rheology of omphacite at high temperature and pressure and significance of its lattice preferred orientations. *Earth and Planetary Science Letters*, *246*(3-4), 432-443.

Table 1. Summary of selected samples for this comparative study, including their paragenesis and the various fracturing patterns identified therein (see text for details on the criteria used for this classification). Numbers in the last three columns refer to the chronological sequence of fracturing events identified in each sample.

	Sample	Region	Pre-fracturing assemblage	Paragenesis associated w/ brittle def.	Fracturing pattern		
					type I	*type II*	*type III*
Polar Urals	PU2	Pus'yerka	white Jd (Jd_1), Ed	Omp, Mg-ktp, Rct, Eck, Phl, Clc		x (1)	x (2)
	PU5	Pus'yerka	white Jd (Jd_1)	Omp, Phl, Clc (±Cal)		x	
	UR11b	Pus'yerka	Ed or Mg-ktp with Omp inc.	Jd_2, Omp, Mg-ktp, Eck/Nyb, Ttn, Chr	x		
	UR03b,03d	Pus'yerka	white Jd (Jd_1)	Jd_2, Omp			x
	UR25	Nephrite brook	white Jd (Jd_1)	Jd_2, Omp, Ttn	x		
Guatemala	MTG00	Motagua region	white Jd	Omp (*not analyzed*)	x		
	MTG01	South Motagua	white Jd (Jd_1)	Jd_2, Omp, Lws, Ttn	x		
	MTG02	South Motagua	white Jd (Jd_1)	Jd_2, Omp, Ttn			x
	MTG03	South Motagua	white Jd (Jd_1)	Jd_2, Omp, Ttn (±REE-rich Ep)		x	
	MTG12	South Motagua	white Jd (Jd_1)	Jd_2, Omp, Ttn		x	
Myanmar	KAS01	Hpakan (Kashin)	white Jd (Jd_1)	Jd_2, Omp, Eck	x (1)		x (2)
	KAS04	Hpakan (Kashin)	white Jd (Jd_1)	Jd_2, Omp, Eck, Clc (±Cls)	x (1)	x (2)	x (3)
	KAS06	Hpakan (Kashin)	Ed (+Omp?)	Jd_2, Omp, Rct, Eck	x		
	KAS07	Hpakan (Kashin)	white Jd (Jd1) and Mg-ktp	Jd_2, Omp, Eck, Chr		x (1)	x (2)
	KAS10	Hpakan (Kashin)	white Jd (Jd_1)	Jd_2, Eck		?	

Table 1

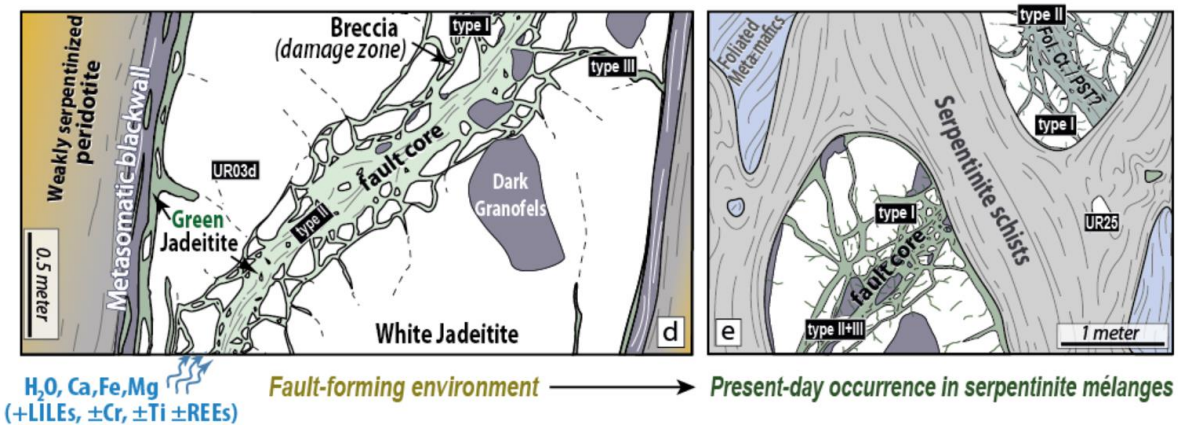
Weakly serpentinized peridotite
Metasomatic blackwall
0.5 meter
Breccia
(damage zone)
type I
type III
UR03d
fault core
Dark Granofels
Green Jadeitite
type II
White Jadeitite
d
Foliated Metamafics
type II
Fol. Cat. pst?
type I
Serpentinite schists
type I
UR25
fault core
type II+III
e
1 meter
H2O, Ca,Fe,Mg
(+LILEs, ±Cr, ±Ti ±REEs)
Fault-forming environment
Present-day occurrence in serpentinite mélanges